Machine learning methods for particle stress development in suspension Poiseuille flows

Amanda A. Howard[1*], Justin Dong[1,2†], Ravi Patel[3†], Marta D'Elia[4], Martin R. Maxey[2] and Panos Stinis[1]

[1]Pacific Northwest National Laboratory, Richland, 99354, WA, USA.
[2]Division of Applied Mathematics, Brown University, Providence, 02912, RI, USA.
[3]Sandia National Laboratories, Albuquerque, 87185, NM, USA.
[4] Pasteur Labs., Brooklyn, 11205, NY, USA.

*Corresponding author(s). E-mail(s): amanda.howard@pnnl.gov;
†These authors contributed equally to this work.

Abstract

Numerical simulations are used to study the dynamics of a developing suspension Poiseuille flow with monodispersed and bidispersed neutrally buoyant particles in a planar channel, and machine learning is applied to learn the evolving stresses of the developing suspension. The particle stresses and pressure develop on a slower time scale than the volume fraction, indicating that once the particles reach a steady volume fraction profile they rearrange to minimize the contact pressure on each particle. We consider the timescale for stress development and how the stress development connects to particle migration. For developing monodisperse suspensions we present a new physics-informed Galerkin neural network that allows for learning the particle stresses when direct measurements are not possible. We show that when a training set of stress measurements is available, the MOR-physics operator learning method can also capture the particle stresses accurately.

Keywords: Stokes flow, Viscous suspensions, Particle dispersion, Machine learning

1 Introduction

Solid-fluid multiphase flows systems occur in many areas of recent interest in both nature and industry, with wide-ranging applications including microfluidic systems for cell sorting and inertial focusing (Di Carlo, 2009), cement processing, food processing (Servais et al., 2002), mud (Coussot, 1994), and sediments. In these applications, it is important to understand the microstructure that appears due to particle stresses with spherical particles at high volume fraction (Morris, 2009), and particle migration and segregation by size or density (Kanehl and Stark, 2015; Lyon and Leal, 1998b; Batchelor and Van Rensburg, 1986; Chang, 1994; Pesche et al., 1998; Pesche, 1998). Such flows represent a complex dynamical system due to the nonlinear coupling of the flow and the particle positions and velocities, which in turn determine the flow.

Early experiments by Gadala-Maria and Acrivos (1980) and later by Leighton and Acrivos (1987) showed that when a gradient exists in the fluid shear rate, suspended particles migrate toward regions of lower shear in a phenomenon called shear-induced migration. Karnis et al.

(1966) found that in a Poiseuille flow in a tube the particles formed a plug at the core of the channel due to shear-induced migration. Similar results are seen in a range of experiments in a channel with both colloidal and non-colloidal particles and with monodisperse particle sizes (Koh et al., 1994; Hampton et al., 1998; Lyon and Leal, 1998a; Butler et al., 1999; Gao et al., 2009; Semwogerere et al., 2007). Shear-induced migration is also seen in oscillating Poiseuille flows of suspensions in a pipe (Snook et al., 2016). Results from experiments reveal that as the particles migrate toward the center of the channel, they create a densely packed plug with volume fraction close to the maximum volume fraction for the system. This high volume fraction causes a blunting or flattening of the parabolic velocity profile at the core of the channel (Lyon and Leal, 1998a). Experimental results have been confirmed by simulations with the Force Coupling Method (FCM) (Yeo and Maxey, 2011) and lattice-Boltzmann simulations (Chun et al., 2017). A series of experiments and simulations have further shown the key role of particle contacts in irreversible particle migration (Da Cunha and Hinch, 1996; Zarraga and Leighton, 2002; Metzger and Butler, 2010; Metzger et al., 2013; Pham et al., 2015, 2016).

Leighton and Acrivos (1987) developed a phenomenological model to explain the shear-induced migration seen in experiments, which relies on irreversible inter-particle interactions. Later models include diffusive flux models (Phillips et al., 1992) and the Suspension Balance Model (SBM) proposed by Nott and Brady (1994), with subsequent refinements by Morris and Boulay (1999); Miller and Morris (2006); Lhuillier (2009); Nott et al. (2011), which have been successful in correlating a number of situations (Boyer et al., 2011; Snook et al., 2016; Kanehl and Stark, 2015; Dbouk et al., 2013). The SBM predicts that particle migration is due to the divergence of the particle phase stress. These models are based on a mean-field, continuum representation and approximation of locally uniform gradients, particle volume fractions, and particle stresses.

The SBM works quite well for monodisperse particle flows (Dbouk et al., 2013). However, the SBM is essentially a point-particle concept with no explicit particle size. Several open issues remain, including how the presence of a wall layer, and the subsequent particle layering that builds upon the wall layer, change the dynamics, as particle stress gradients and volume fraction profiles will have sharp discontinuities at the wall layer. In addition, in the channel core of a Poiseuille flow the shear stress drops to zero, which requires careful handling in SBM. Additionally, there can be cases where fronts occur on the scale of the particle size, which is not accounted for in SBM. An open question is what aspect of the particle stress controls the migration flux, and how to link averaged results to individual particle interactions. Given that the SBM works quite well, this raises the question of how we can use the SBM to learn the particle stress from noisy data available from experiments and simulations. To answer this question, in this work we turn to machine learning.

Recently, utilizing neural networks to approximate partial differential equations (PDEs) has gained much attention in the scientific computing, machine learning, and engineering communities for problems that have traditionally been in the domain of computational scientists and numerical analysts, for instance see Raissi et al. (2019); Yu et al. (2018); Sirignano and Spiliopoulos (2018); Karniadakis et al. (2021) and the references therein. For complex systems, it can be necessary to use an operator learning method, including operator inference (Peherstorfer and Willcox, 2016), Deep Operator Networks (Lu et al., 2021), or Fourier Neural Operators (Li et al., 2021). Our recent work has successfully used a physics-informed neural network (PINN), along with FCM data, to learn the viscosity of a densely packed monodisperse suspension in steady state (Reyes et al., 2021). Others have been able to accurately learn the variable drag forces on suspended spherical particles (He and Tafti, 2019), predict the rheological properties of a suspension of fibers (Boodaghidizaji et al., 2022), and learn the lubrication correction for coupled DPD–DEM simulation of colloidal suspensions (Wang et al., 2021). In this work, we apply the Modal Operator Regression (MOR-Physics) operator learning framework (Patel and Desjardins, 2018; Patel et al., 2021) to obtain a model for the particle stresses in developing monodisperse and bidisperse suspensions. When an accurate physics-based model, such as the SBM, is available, we can apply physics-informed training. For this purpose, we utilize the Galerkin Neural Network framework introduced in Ainsworth and Dong (2021), the advantage of which is that it allows for high-order approximation of PDEs by generating highly adaptive basis functions with which to approximate their solutions.

In this paper, we consider developing monodisperse and bidisperse Poiseuille flows. In contrast to previous studies, which looked at a final steady state Poiseuille flow once the stress and volume fraction profiles have reached a steady state (Yeo and Maxey, 2011), the developing Poiseuille flow data can help elucidate questions as to the primary factors driving particle migration in a channel. In Sec. 2 we describe the numerical method used in the simulation data. Sections 3 and 4 describe the evolution of the particle volume fractions and fluxes for monodisperse and bidisperse flows, respectively, to establish the stress development patterns we wish to recover with machine learning. We then discuss two methods for learning and predicting the particle stresses as the suspension develops. When available suspension balance models can accurately capture the stresses, physics-informed neural networks are able to accurately predict the particle stress, as shown in Sec. 5. However, when physics-based models do not capture the bidisperse suspension stresses, the MOR-Physics operator learning method is needed in Sec. 6.

2 Numerical method for suspension flow simulations

The simulations in this paper are completed using the Force Coupling Method (FCM). Developed by Maxey and Patel (2001); Lomholt and Maxey (2003), the FCM is used to simulate a large number of densely packed hard spherical particles in a wide range of applications, including high volume fraction fluid flow in a channel (Yeo and Maxey, 2011, 2010a), the settling of particles with bidispersed sizes (Abbas et al., 2006) or weights (Howard et al., 2018), and the coagulation of platelets in blood flow (Pivkin et al., 2006). Incorporation of lubrication forces allows for simulations of very densely packed particles with bulk volume fraction $\phi_B > 0.2$ (Dance and Maxey, 2003; Yeo and Maxey, 2010b). Provided here is an overview of FCM as it is implemented for the simulations discussed in this work. For more complete details, please see Yeo (2011) and Yeo and Maxey (2010b).

In simulations, the contact force models the particle surface roughness as well as numerically preventing the particles from overlapping. While the lubrication forces between two spheres will theoretically prevent the particles from touching, in simulations some form of a contact force is needed to prevent particle overlaps due to the discrete time step. In the FCM, the contact force between two particles is modeled by a short-range force that acts along the line of the centers of the particles and depends only on the particle sizes and the distance between the two particles (Yeo and Maxey, 2010b). This force is zero when the particles are separated by more than a small distance, typically a gap width of less than 0.05% of a particle radius. Based on the work of Yeo and Maxey (2010b), the following contact force model for the force on particle j due to particle i, with centers at $\mathbf{r}_j$ and $\mathbf{r}_i$ and radii a_j and a_i, is considered:

$$F^C_{ij} = \begin{cases} -6\pi\mu\bar{a}_{ij}F_{ref}\left(\frac{R^2_{ref}-r^2}{R^2_{ref}-4\bar{a}^2_{ij}}\right)^6 \frac{\mathbf{r}_{ij}}{r}, & r \leq R_{ref} \\ 0, & \text{otherwise} \end{cases} \tag{1}$$

Here, $\bar{a}_{ij} = \frac{1}{2}(a_i + a_j)$, $\mathbf{r}_{ij} = \mathbf{r}_j - \mathbf{r}_i$, $R_{ref} = 2.01\bar{a}_{ij}$ is the contact force cutoff distance, $r = |\mathbf{r}_{ij}|$, and $F_{ref} = 100$ is a parameter chosen to control the minimum separation of the particles. The fluid viscosity is $\mu = 1$.

The phasic average of a variable $\mathbf{g}$ is defined as (Drew, 1983; Yeo and Maxey, 2011),

$$\langle \mathbf{g}\chi_p\rangle(y) = \frac{1}{H_x \times H_z}\left\langle \sum_{i=1}^{N_p} \mathbf{g}^i \chi^i_p(\mathbf{x})\, dx\, dz \right\rangle, \tag{2}$$

where χ^i_p is the indicator function of the ith particle and $\mathbf{g}^i$ is the ith particle's value of $\mathbf{g}$. The particle phase average of $\mathbf{g}$ can then by found by

$$\langle \mathbf{g}\rangle(y) = \frac{\langle \mathbf{g}\chi_p\rangle(y)}{\phi(y)}. \tag{3}$$

The particle pressure is defined as the trace of the stress tensor from the elastic contact force, S^C_{ij}:

$$\Pi = -\frac{1}{3}\left(S^C_{11} + S^C_{22} + S^C_{33}\right). \tag{4}$$

In this work, we will solve FCM in a channel with planar, no-slip walls separated by a distance H_y. Periodic boundary conditions are applied in the streamwise (z, denoted by subscript 3) and spanwise (x, denoted by subscript 1) or vorticity direction of the mean flow. All distances are nondimensionalized by the particle radius for monodisperse simulations and the largest particle radius in bidisperse simulations, denoted by a. The wall-normal direction y is denoted by subscript 2. A channel half height of $h = 20a$ is used in the simulations, resulting in a channel height $H_y = 40a$. The channel depth is $L_x = 30a$, and the channel length is $L_z = 60a$ for monodisperse simulations and $L_z = 30a$ for bidisperse simulations. The bulk volume fraction is fixed at $\phi_B = 0.4$. A constant pressure gradient of $f^D = \frac{\partial p}{\partial z} = 0.0288$ is imposed on the flow, which sets the streamwise fluid velocity in the absence of embedded particles. The pressure gradient is chosen so that the average bulk velocity of the particles in the streamwise direction at steady state is on the order of one. The streamwise bulk particle velocity varies in response to the imposed pressure gradient depending on the local volume fraction. We scale the particle stresses and contact pressure by the wall shear stress, $\sigma_w = f^D h$. For bidisperse simulations, the particle size ratio is denoted by $\lambda = a_S/a_L$, where a_S and a_L are the radii of the small and large particles, respectively. The relatively small particle volume fraction is denoted by $\beta = \phi_S/\phi_B$, where ϕ_S is the volume fraction of small particles and ϕ_B is the total volume fraction of small and large particles.

The simulations are started from a random configuration of particles. Particles with a radius $0.85a_i$ are placed in a channel with random coordinates. Then, a molecular dynamics simulation is run as the particle size is slowly increased to a_i over 1,000 time steps. At high volume fractions, randomly placing full-size particles in a channel without the inflation step is time prohibitive, as it can take many, many iterations to find an empty location for each particle. This two-step process allows for a uniform volume fraction across the channel, although some layering does occur at the channel walls due to the inflation procedure.

The accumulated strain is defined as

$$\gamma = \frac{\overline{u_z} t}{h},$$

where $\overline{u_z}$ is the particle bulk velocity in the streamwise direction. At a bulk particle volume fraction of $\phi_B = 0.4$, the bulk particle velocity increases to a steady value of $\overline{u_z} = 1.28$ over about 250–300 strain units for monodisperse simulations and $\overline{u_z} = 1.21$ for bidisperse simulations with $\beta = 0.25$, $\overline{u_z} = 1.17$ with $\beta = 0.5$, and $\overline{u_z} = 1.14$ with $\beta = 0.75$.

2.1 Reseeding procedure

The FCM simulations presented in this paper represent a significant amount of computational time due to the long time to steady state for dense suspensions in Stokes flow. Due to this, to achieve better statistical averaging for profiles of rheological parameters we use a procedure to restart the flow after "jiggling" the particles slightly. The restarted flows are run for ten strain units, and then an ensemble average is taken over the reseeded flows. This allows us to attain averaged profiles without having to run the full simulation several times and reduces the computational cost by about 90% compared with running a full simulation from $\gamma = 0$. The reseeding and averaging procedure offers additional insights into the dynamics of a developing suspension as well as provides a greater understanding of the forces significant in particle migration.

The reseeding procedure is completed as follows. A snapshot of the particle locations is taken at a given accumulated strain, γ. The particles are then randomly moved a small displacement from their locations. This displacement disrupts the particle-particle contacts and force chains that may have formed up until this point in the simulation. The flow is then restarted and run for ten strain units. When indicated, the results in this paper are averaged over four reseeded simulations.

The reseeding procedure in itself reveals interesting properties of the suspension dynamics, which we illustrate by simulating a monodisperse suspension with radius $a = 1$ and $\phi_B = 0.4$. As an example, in Fig. 1 the reseeding occurs at $\gamma = 250$, with averages taken at $\gamma = 260$. One quantity of interest is the separation distance, defined as the particle displacement between the original flow and the reseeded flow, denoted by the superscript $*$, to give $S(t) = \sqrt{\frac{1}{N_p}\sum_{i=0}^{N_p}\left[(x_i(t) - x_i^*(t))^2 + (y_i(t) - y_i^*(t))^2\right]}$. The average particle displacement after the reseeding occurs is $\langle S(0) \rangle = 0.0077a$. As the simulation progresses, the separation distance increases.

Fig. 1 also shows the development of the pressure profile. The pressure profile is averaged over five reseeded simulations. The resulting profile shows similar features to the original suspension profile, but the averaging removes some of the noise present in the original simulation. The reseeding procedure disrupts the particle contacts, resulting in zero contact pressure when a reseeded simulation is started. The contact pressure redevelops over the first strain unit of the reseeded simulations. Over the next ~ 2 strain units the average particle pressure remains very similar to that of the original suspension. After ten strain units, the chaotic nature of the dense suspension is visible and the averaged particle pressure is random.

The reseeding procedure can also give insight into the differences between oscillating suspension flows, such as those considered by Snook et al. (2016); Metzger and Butler (2012); Cui et al. (2017); Howard and Maxey (2018); Antolik et al. (2023) and flows driven by a constant pressure gradient, such as those in this paper and in Yeo and Maxey (2011, 2010a), by giving a time scale for the pressure to develop from an initially static simulation of about one strain unit. Thus, we can consider that an oscillating flow with a strain amplitude of significantly more than one strain unit should have the same behavior as that of a steady flow.

In this work we average over four reseeded simulations and we denote averaged quantities by the notation $(\cdot)^*$. Reseeded profiles at accumulated strain γ_0 are reseeded at $\gamma = \gamma_0 - 10$, then the simulation is run for 10 strain units with the new particle configuration to produce averaged profiles in this paper. For this reason, at $\gamma = 0$ we do not use averaged profiles.

3 Monodisperse suspension stress development

In this section, we discuss the development of a monodisperse suspension with bulk volume fraction $\phi_B = 0.4$. We begin by considering the particle volume fraction, given in Fig. 2 to provide a timeline for the particle migration. At the initial

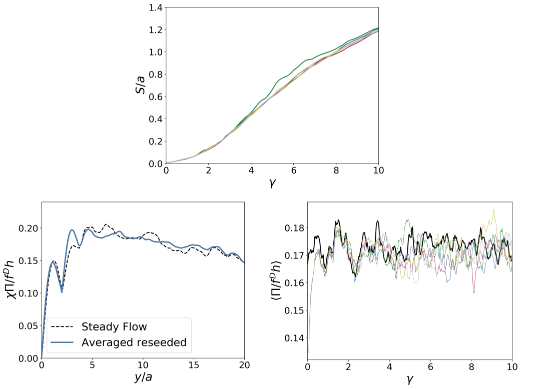

Fig. 1: Example of the effects of the reseeding procedure. (Top): Development of the separation distance S for five reseeded simulations, plotted versus accumulated strain. (Bottom left): Pressure profile for the original steady flow simulation and averaged pressure profile from five reseeded suspensions. (Bottom right): Bulk pressure development of the steady and reseeded suspensions, plotted versus accumulated strain.

time, $\gamma = 0$, the volume fraction is approximately uniform across the channel. There is some particle layering visible at the walls, located at $y/a = 1$, due to the procedure used to initialize the particle locations. Subsequent layers are visible at $y/a = 3$ and $y/a = 5$, which build on the initial wall layer. This wall layering has been seen experimentally in Snook et al. (2016); Sarabian et al. (2019).

As the flow develops the wall layers drop slightly in volume fraction, with the largest changes occurring in the initial ~ 120 strain units. There is a large migration to the centerline, with a noticeable increase in volume fraction in the first forty strain units. The bulk of the migration towards the centerline occurs before $\gamma \approx 260$, although small changes do occur in the next four hundred strain units. This suggests that the particle migration occurs predominantly in the first couple hundred strain units for this volume fraction.

The short-range contact force generates a contact pressure, shown in Fig. 3. The contact pressure is initially zero across the channel, as no contacts have developed between the particles. After forty strain units, the contact pressure reaches the maximum value near the channel walls and begins to increase at the channel centerline. Over

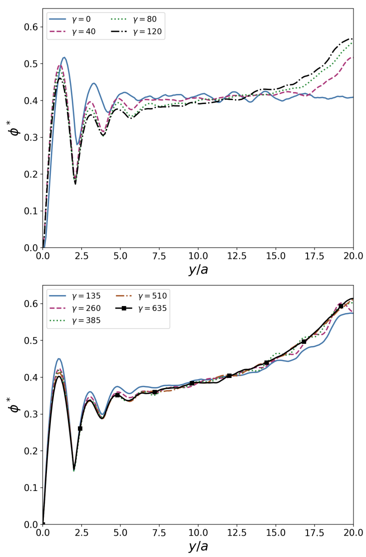

Fig. 2: Volume fraction profiles at accumulated strain $\gamma = 0 - 635$ for a monodisperse suspension with $\phi_B = 0.4$. The volume fraction is averaged over the channel center line at $h = 20.0a$. The $(\cdot)^*$ notation denotes the profile is averaged over four reseeded simulations, as discussed in Sec. 2.1.

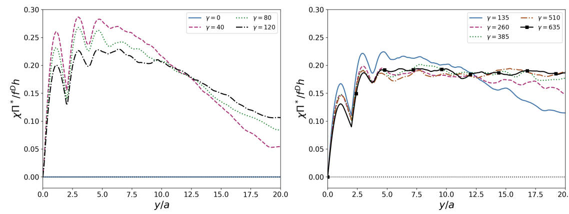

Fig. 3: Averaged particle contact pressure profiles as defined by Eq. 4 for a monodisperse suspension with $\phi_B = 0.4$ at accumulated strain $\gamma = 0 - 635$. The profiles are averaged over the channel center line at $h = 20.0a$.

time, the contact pressure continues to increase at the centerline and decrease near the walls, until it reaches a profile that is approximately uniform across the channel, except for two layers at the wall where the pressure drops due to the particle layering.

Gradients in the contact pressure are indicative of particle movements, with particles moving from areas of high contact pressure to low contact pressure. By comparing the changes in the volume fractions in Fig. 2 and the contact pressure in Fig. 3, these contact pressure profiles are consistent with an average particle migration to the centerline, especially when $\gamma < 260$. The largest particle migration occurs early in the simulation, where there is a large gradient in the contact pressure, driving the particles toward the centerline. As the contact pressure reaches an equilibrium the particle migration slows, with minimal changes in the volume fraction profile after $\gamma = 385$. Interestingly, the equilibrium in the particle contact pressure is reached after the volume fraction profile ceases to evolve, suggesting that once the steady-state volume fraction profile is reached the particles continue to rearrange into a more stable state, equalizing the pressure between pairs of particles.

The total particle stress, which contains the contributions from the FCM longer range hydrodynamic stresslet, lubrication stresslet, and contact stresses, is shown in Fig. 4. These stresses follow a similar trend to the particle contact pressure, where the largest magnitude values are found at short times, then the stresses relax to an equilibrium value across the channel. The wall layering is apparent, and at later times the stress is lowest in magnitude near the wall. The stresses increase slightly after $\gamma = 385$, although the largest change is seen before $\gamma = 260$.

The normal stress differences are defined as $N_1 = \sigma_{33} - \sigma_{22}$ and $N_2 = \sigma_{22} - \sigma_{11}$, and are shown in Fig. 5. The first normal stress difference is positive, while the second is negative. Since the stresses σ_{ii} are all negative, a positive first normal stress difference means $|\sigma_{22}| > |\sigma_{33}|$ and the negative second normal stress difference means $|\sigma_{22}| > |\sigma_{11}|$, as can be verified in Fig. 4. The wall-normal stress σ_{22} supports a pressure from the walls, supporting the development of the particle migration.

The particle shear stresses are shown in Fig. 6. These profiles have small differences from those in Yeo and Maxey (2011) due to the correction of a typographical error in the data output processing in the FCM code. The slope in the corrected profiles is negative across the channel outside of the area near the walls in which layering occurs.

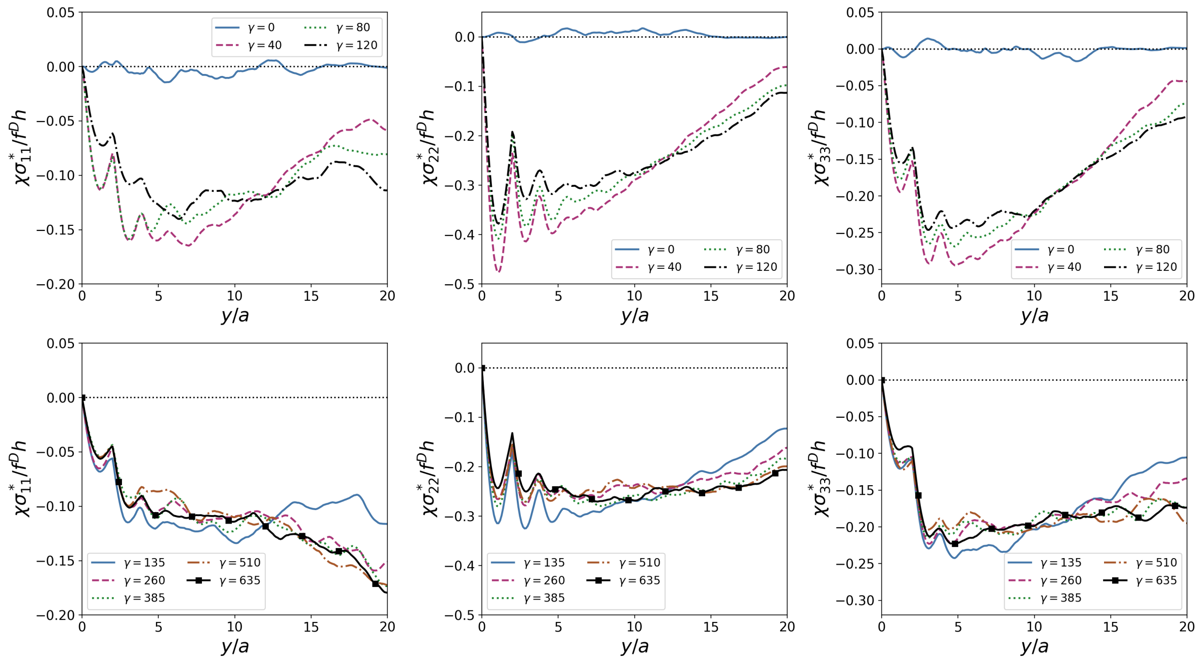

Fig. 4: Averaged stress profiles σ_{11}^* (left), σ_{22}^* (middle), and σ_{33}^* (right) for monodisperse flows of particles with $\phi_B = 0.4$ for $\gamma = 0 - 635$. The profiles are averaged over the channel center line at $h = 20.0a$.

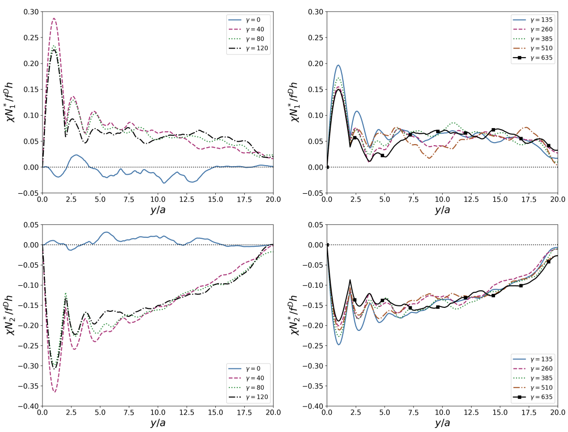

Fig. 5: Averaged normal stress differences N_1^* (top) and N_2^* (bottom) for a monodisperse suspension with $\phi_B = 0.4$. The profiles are averaged over the channel center line at $h = 20.0a$.

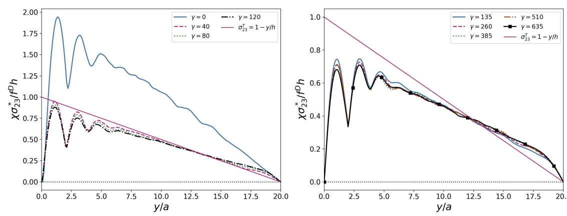

Fig. 6: Averaged shear stress profiles σ_{23}^* for monodisperse flows of particles with $\phi_B = 0.4$ for $\gamma = 0 - 635$. The profiles are averaged over the channel center line at $h = 20.0a$. The total stress $\sigma_{23}^T = 1 - y/h$ is the expected sum for all stress contributions in the continuum, stationary state limit. Departures can arise from finite particle size effects.

4 Bidisperse suspension stress development

While monodisperse suspensions have been relatively well studied, much less is known about bidisperse suspension Poiseuille flows at even relatively large particle size ratios, $\lambda = a_S/a_L$, where the subscript S will refer to quantities relating to small particles and the subscript L will refer to those relating to large particles. We nondimensionalize by the large particle radius, $a = a_L$. In this section, we will discuss the stress development for a particular bidisperse suspension, with $\lambda = 0.6$, $\phi_B = 0.4$, and relative volume fraction of small particles, $\beta = \phi_S/\phi_B = 0.75$. In the interest of space, two additional cases, with $\beta = 0.5$ and $\beta = 0.25$, are shown in Appendix A.1. The flow begins with particles uniformly seeded in a channel with width $H_y = 40a$.

Previous work has shown that in bidisperse Poiseuille flows the large particles congregate in the center of the channel (Graham et al., 1991; Husband et al., 1994; Lyon and Leal, 1998b; Semwogerere and Weeks, 2008; Gao et al., 2009; Kanehl and Stark, 2015; Schroen et al., 2017; Chun et al., 2019). This is due to the increased velocity with which large particles migrate toward the channel center due to their larger relative size. Some work has referred to this as segregation, where small particles are excluded from the center region. However, without Brownian forces, we see large particle enrichment at the channel centerline, as in Fig. 7, but not segregation because there is no mechanism by which to remove the small particles from the center of the channel. This is most clearly seen in Fig. 28 with $\beta = 0.5$. While the small and large volume fractions begin equal across the channel in the flow in Fig. 28, the large particle volume fraction is higher at the centerline at a larger accumulated strain.

The particle stresses are calculated as the total contribution to the stress of each phase due to the other phases, so the small particle stress contains the total of all interactions with large and small particles, and the same for the large particles. The particle contact profiles in Fig. 8 show large deviations from the monodisperse contact pressure profiles in Fig. 3. The contact pressure is very large at the channel centerline, and examination shows that the large particle pressure is due to the contribution from small particles. The large particle contact pressure becomes uniform across the channel as the flow develops, as in the monodisperse case. The larger pressure contribution from the small particles is again particularly apparent in Fig. 29 with $\beta = 0.5$. While outside the center and wall regions, the contact pressures are approximately equal for small and large particles, at the centerline the small particle contact pressure is significantly higher than the large particle contact pressure.

In our earlier work with bidisperse suspensions in Couette flows, we found that the individual components of the particle stress scale according to the relative volume fractions of small and large

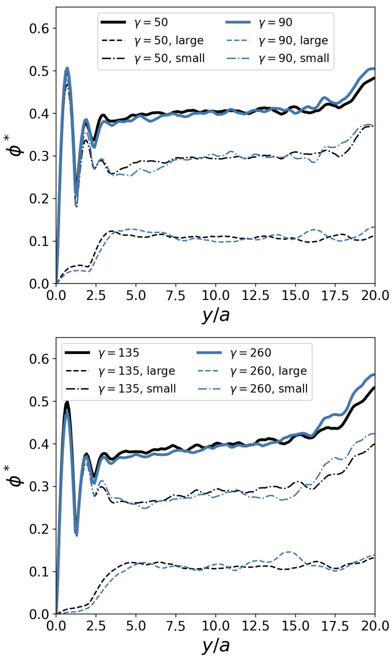

Fig. 7: Averaged volume fraction profiles at accumulated strain $\gamma = 0 - 260$ for a bidisperse suspension with $\phi_B = 0.4$, $\lambda = 0.6$, and $\beta = 0.75$ for the full suspension (solid lines), large particles (dashed lines), and small particles (dash-dotted lines). The volume fraction is averaged over the channel center line at $y = 20.0a_L$. The $(\cdot)^*$ notation denotes the profile is averaged over four reseeded simulations, as discussed in Sec. 2.1.

particles. That is, $\langle\sigma_{ii}^S\rangle/\langle\sigma_{ii}^L\rangle \approx \phi_S/\phi_L$ (Howard et al., 2022). In contrast, examination of the individual components of the particle stresses in Poiseuille flow, in Fig. 9, shows that the small particles develop a very large excess stress at the centerline, especially when compared to the large particle stresses. One explanation for this is a possible caging effect on the small particles near the centerline. As the large particles migrate towards the center, they exert large forces on the small particles and trap the small particles at the center of the channel.

The normal stress differences, given in Fig. 10 have $N_1 > 0$ and $N_2 < 0$, as previously shown for monodisperse suspensions, and again this is attributed to the nonuniform particle concentration.

The total shear stress profiles, Figs. 11, 30, and 35 have a very similar shape as the monodisperse

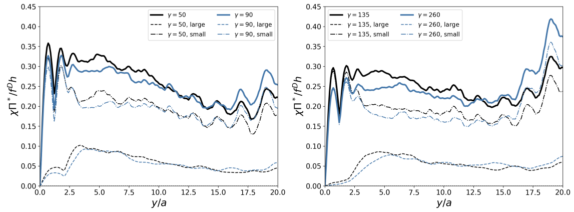

Fig. 8: Averaged particle contact pressure profiles as defined by Eq. 4 at accumulated strain $\gamma = 0 - 260$ for a bidisperse suspension $\phi_B = 0.4$, $\lambda = 0.6$, and $\beta = 0.75$. The profiles are averaged over the channel center line at $y = 20.0a_L$.

shear stress profiles in Fig. 6. The total shear stress scales as $\chi\sigma_{23}/f^D h \sim 1-y/h$, and the slope is negative throughout the channel, excluding the wall region. The contributions to the shear stress scale as $\chi\sigma_{23}^S/f^D h \sim \beta(1-y/h)$ for the small particles and $\chi\sigma_{23}^L/f^D h \sim (1-\beta)(1-y/h)$ for the large particles. What is interesting is that the small excess in the shear stress above the scaling line at the center of the channel is caused by the contribution from the small particles for all three values of β.

5 Physics-informed machine learning with the suspension balance model

5.1 Particle fluxes and the suspension balance model

The suspension balance model (SBM) from Morris and Boulay (1999) begins with the mass conservation equation

$$\frac{\partial \rho}{\partial t} + \nabla \cdot (\rho \mathbf{u}) = 0 \tag{5}$$

and momentum conservation equation

$$\rho \left(\frac{\partial \mathbf{u}}{\partial t} + \mathbf{u} \cdot \nabla \mathbf{u} \right) = \nabla \cdot \sigma + \mathbf{b} \tag{6}$$

where ρ is the mass density, $\mathbf{u}$ is the pointwise velocity, σ is the stress tensor, and $\mathbf{b}$ are the body and interparticle forces. By an averaging procedure (Drew and Lahey, 1993), we get the particle-phase conservation equations (Morris and Boulay, 1999):

$$\frac{\partial \phi}{\partial t} + \nabla \cdot (\mathbf{U}\phi) = 0 \tag{7}$$

$$\rho_p \frac{D_p(\mathbf{U}\phi)}{Dt} = \nabla \cdot \Sigma_p + n\langle \mathbf{F}^H \rangle_p + \langle \mathbf{b} \rangle_p \tag{8}$$

where $\mathbf{U}$ is the local average particle phase velocity, $\frac{D_p(\mathbf{U}\phi)}{Dt} \equiv \frac{\partial}{\partial t} + \mathbf{U} \cdot \nabla$, $\mathbf{F}^H$ is the hydrodynamic force on a particle, $\langle \cdot \rangle_p$ denotes a particle-phase average, and n is the particle number density. Σ_P is the particle phase stress. For Stokes flow with neutrally buoyant particles, Eq. 8 reduces to

$$\nabla \cdot \Sigma_p - \frac{9\eta_f}{2a^2} \phi f^{-1}(\phi) \left(\mathbf{U} - \langle \mathbf{u} \rangle \right) = 0 \tag{9}$$

where f is the sedimentation hindrance function, discussed below, and η_f is the viscosity of the suspending fluid. The particle flux $\mathbf{j}$ is defined as $\mathbf{j} = \phi \mathbf{U}$. Eq. 9 can be rearranged to give the particle migration flux, or the flux of particles relative to the suspension mean flow, as:

$$\mathbf{j}_\perp \equiv \phi \mathbf{U} - \phi \langle \mathbf{u} \rangle = \frac{2a^2}{9\eta_f} f(\phi) \nabla \cdot \Sigma_p. \tag{10}$$

The hindrance function, $f(\phi)$, is taken from Richardson and Zaki (1954)

$$f(\phi) = (1-\phi)^\alpha.$$

When not mentioned otherwise, we take $\alpha = 5$ as in Boyer et al. (2011). We will explore the impact of varying α in Sec. 5.2.

Eq. 10 relates the particle-phase fluxes and particle-phase stresses. In simulations, we can measure both the particle stresses and fluxes easily. However, in experiments, it is significantly harder to measure the particle stresses. In this section we will first consider the forward problem, going from measurements of the stresses to measurements of the fluxes, which can be computed directly by replacing the particle-phase stress Σ_P in Eq. 10 by the 22−component of the FCM stress tensor, σ_{22}, giving

$$\mathbf{j}_\perp^{FCM} \approx \frac{2a^2}{9\eta_f} f(\phi) \frac{\partial \sigma_{22}}{\partial y} \tag{11}$$

where $\mathbf{j}_\perp^{FCM}$ is the particle-phase flux. We will calculate both the right-hand side and left-hand side

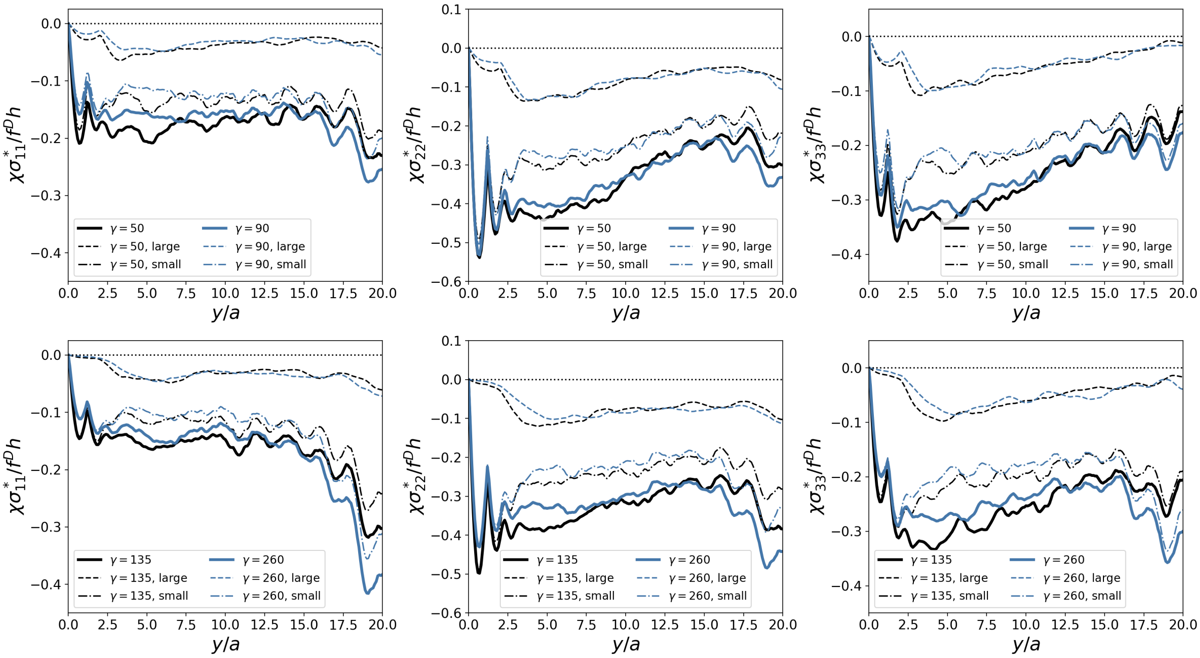

Fig. 9: Averaged stress profiles σ^*_{11} (left), σ^*_{22} (middle), and σ^*_{33} (right) for a bidisperse flow of particles for $\phi_B = 0.4$, $\lambda = 0.6$, and $\beta = 0.75$, and for $\gamma = 50$ and 90 (top row) and $\gamma = 135$ and 260 (bottom row). The profiles are averaged over the channel center line at $y = 20.0a_L$.

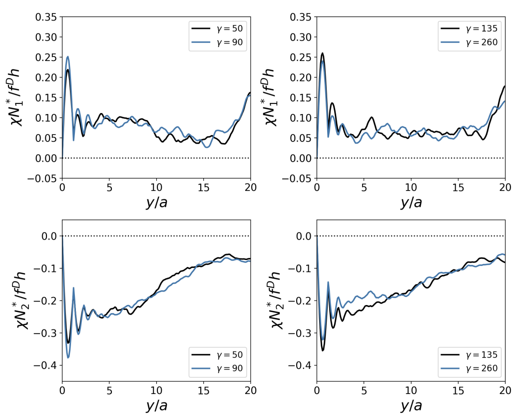

Fig. 10: Averaged normal stress difference profiles N^*_1 (top) and N^*_2 (bottom) for bidisperse flows of particles for $\phi_B = 0.4$, $\lambda = 0.6$, and $\beta = 0.75$. The profiles are averaged over the channel center line at $y = 20.0a_L$.

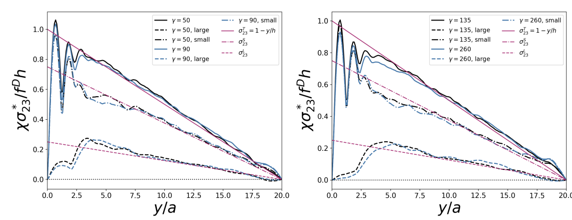

Fig. 11: Averaged shear stress profiles for a bidisperse suspension with $\phi_B = 0.4$, $\lambda = 0.6$, and $\beta = 0.75$. The equation for the line σ^S_{23} is given by $\sigma^S_{23} = \beta(1 - y/h)$ and the equation for the line σ^L_{23} is given by $\sigma^L_{23} = (1 - \beta)(1 - y/h)$. The profiles are averaged over the channel center line at $y = 20.0a_L$.

of Eq. 11 and show that they are in good agreement. In the next section, we will consider the inverse problem, where the particle-phase stress tensor is computed from the particle fluxes using machine learning. Due to the noisy data, directly finding the stresses from the flux by solving Eq. 10 is unreliable.

The averaged profiles presented in Secs. 3 and 4 provide insights into averaged suspension dynamics, however, this requires a large enough dataset to average over and represents a significant computational time. In this work, a goal was to develop methods to learn particle stresses using a minimal amount of data, from one simulation or experiment. In this way, experiments do not need to be repeated several times to generate averaged profiles. For the rest of the paper, we consider methods that use only a single simulation, either monodisperse or bidisperse, as the training data to generate results.

The SBM formulation in Eq. 11 requires taking the derivative of σ_{22}, which is numerically difficult due to the chaotic nature of the particle migrations causing the stress profiles from a single simulation to be quite noisy. To take the derivative, we fit a twentieth-degree polynomial to σ_{22} using the `polyfit` function in the `numpy` Python library (Harris et al., 2020), see Figure 12. Then, the derivative of the resulting polynomial can be taken. A comparison of the particle fluxes computed directly from the FCM simulations and from the SBM is given in Fig. 13. The two quantities agree in magnitude, and both go to zero at the channel centerline, as is expected due to the symmetry of the flow. The SBM does not take into account layering at the channel walls, so the approximations are clearly not accurate in a region near the wall where the stress tensor has a large gradient. Because of the subsequent layering that builds atop the wall layering, the fluxes calculated from the stress tensor are not valid within a region of $\sim 5a$ from the channel wall. To quantify the agreement between the particle flux measured from the FCM simulations and the particle flux calculated with the SBM using the FCM stress tensor, we define the root mean square error (RMSE):

$$RMSE \colon = \sqrt{\frac{1}{n_g}\sum_{i=1}^{n_g}\left[\mathbf{j}_\perp^{FCM} - \mathbf{j}_\perp^{SBM}\right]^2} \qquad (12)$$

where n_g is the number of grid points from $y/a = 5$ to $y/a = 20$ at which the fluxes are calculated, set at 75. The resulting RMSE, averaged over 58 accumulated strain values evenly distributed in $\gamma \in [5, 120]$ is $2.99 \times 10^{-4} \pm 4.94 \times 10^{-5}$. If the RMSE is instead calculated over $10 \leq y/a \leq 20$, the resulting error is $2.13 \times 10^{-4} \pm 5.42 \times 10^{-5}$, indicating that the average error is slightly lower in the bulk region of the channel and further from the channel walls. In Fig. 14 we give a comparison between the predicted and measured flux values.

Overall, the SBM using the FCM stress tensor captures the general features of the particle flux profile for $0.5 < y/h < 1$. This suggests that the SBM as written is accurate for FCM data when $\Sigma_P = \sigma_{22}$, and sets us up to consider the problem of learning the particle phase stress, σ_{22}, when measurements are not available.

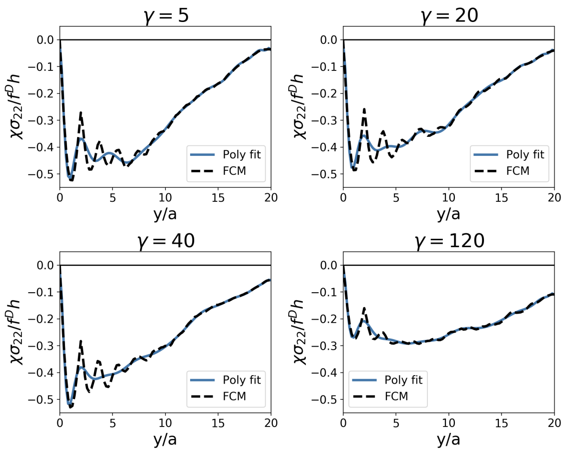

Fig. 12: Monodisperse stress profiles used in Eq. 11, and the polynomial fits used to calculate the derivative.

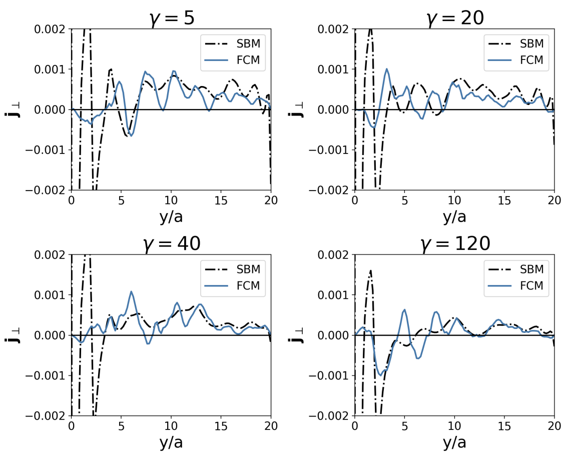

Fig. 13: Monodisperse particle fluxes from the FCM simulations (left-hand side of Eq. 11, solid blue lines) and from the SBM with $\Sigma_P = \sigma_{22}$ (right-hand side of Eq. 11, dash-dotted black lines).

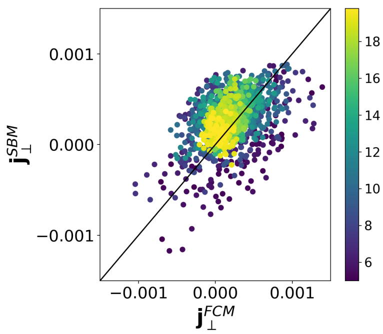

Fig. 14: A comparison between particle fluxes from the FCM simulations (left-hand side of Eq. 11, $\mathbf{j}_\perp^{FCM}$) and from the SBM (right-hand side of Eq. 11, $\mathbf{j}_\perp^{SBM}$), for $5 \le \gamma \le 120$. The symbol color corresponds to the y-coordinate at which the flux is calculated, $5 \le y/a \le 20$. The line $y = x$ is provided for reference.

5.2 Learning the stress in monodisperse suspensions

Knowing that the FCM simulations agree well with the model proposed by Morris and Boulay (1999), in the next section we consider how we can use the SBM paired with simulation data of just the particle fluxes and volume fractions to learn the particle stresses using a newly developed machine learning method called physics-informed Galerkin Neural Networks (Ainsworth and Dong, 2021). While this is not strictly necessary for FCM, because we can directly output the stresses from the simulation data, this technique could be applied to experimental data, where it is not possible to measure the particle stresses directly. By learning the stress profiles from quantities that are easier to measure in a laboratory, we can approximate the stress profiles in experiments where they would otherwise be unknown.

We are interested in comparing the continuum scale dynamics of the SBM formulation with the particle scale dynamics of the FCM. To this end, we approximate the stress Σ_p in Eq. 10 and compare it with the stress obtained from the FCM. We again approximate Σ_p by the stress component σ_{22}. Thus, in order to approximate Eq. 10, we must solve the boundary-value PDE:

$$\begin{cases} \dfrac{2a^2}{9\eta_f} f(\phi) \dfrac{\partial \sigma_{22}}{\partial y} = \mathbf{j}_\perp^{FCM} & \text{in } \Omega \\ \sigma_{22}|_{y=y_0} = g & \text{on } \Gamma. \end{cases} \tag{13}$$

Here, $\Omega = (\epsilon, H_y - \epsilon) \times (0, H_\gamma)$ is the space-time computational domain with H_γ being the maximum strain unit and $\epsilon = 5a$ being a small perturbation away from the channel walls since the SBM formulation does not take into account layering at the channel walls. The boundary is denoted by $\Gamma = \{\epsilon\} \times (0, H_\gamma)$ while the function $g(\gamma)$ serves as a boundary condition. We take the maximum strain $H_\gamma = 200$, as after $\gamma = 200$ the particle fluxes are much smaller in magnitude.

To approximate Eq. 13 using Galerkin Neural Networks, we represent the solution σ_{22} as a linear combination of hierarchical basis functions $\{\Sigma_i^{NN}\}_{i=1}^n$, each of which is the output of a shallow feedforward neural network:

$$\sigma_{22}^{GNN}(y, \gamma) \approx \sum_{i=1}^{n} c_i \Sigma_i^{NN}(y, \gamma). \tag{14}$$

We note that Eq. 13 requires the boundary data g to be well-posed. This data could be taken as the stress value from Morris and Boulay (1999), or other stress measurements. We use the boundary values of the FCM stress σ_{22} as the boundary condition. More mathematical details of the Galerkin Neural Network framework may be found in Appendix A. To train, we first train a GNN to represent the volume fraction profile, ϕ^{GNN}, shown in Fig. 15. Then, this network is used in conjunction with the simulation flux profile to find the stress profile, given by Eq. 14, that best satisfies Eq. 13. When the learned stress profile σ_{22}^{GNN} is used to evaluate Eq. 13 with ϕ^{GNN} as the volume fraction, the resulting flux, denoted by $\mathbf{j}_\perp^{GNN}$, should agree well with $\mathbf{j}_\perp^{FCM}$.

We first consider the monodisperse suspension. The viscosity of the fluid is taken to be $\eta_f = 1$. We utilize seven basis functions to approximate the stress. Each basis function is represented by a neural network consisting of two hidden layers and $20 \times 2^{i-1}$ neurons per layer; the activation function used for all basis functions is `tanh`; and the training data consists of 256×128 Gauss-Legendre quadrature points in the (y, γ) Cartesian plane.

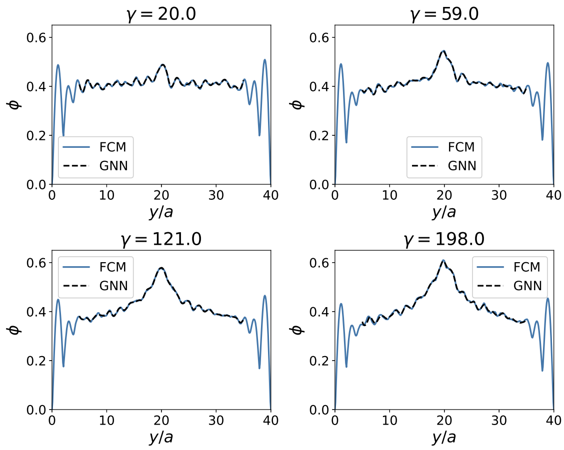

Fig. 15: Volume fraction profiles for the monodisperse suspension from the FCM and learned volume fraction profile from the GNN formulation at $\gamma = 20, 59, 121, 198$.

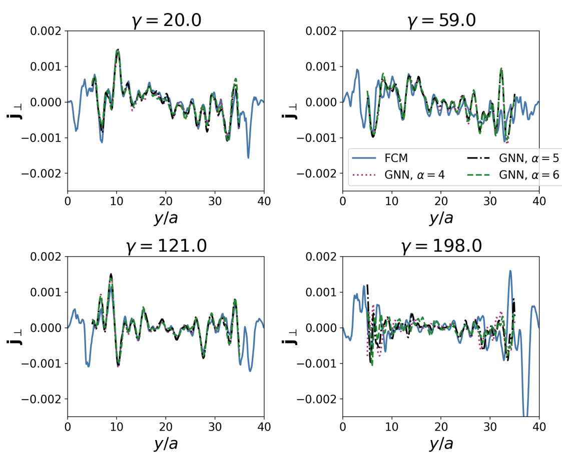

Fig. 16: Flux profiles for the monodisperse suspension from the FCM and learned stress from the GNN formulation at $\gamma = 20, 59, 121, 198$.

Figures 16 and 17 provide one-dimensional profiles of the stress and flux for selected strain values. The stress profiles generated by solving Eq. 10 using the Galerkin neural network framework properly capture the general features of the stress for early and moderate strains. The most accurate results are clearly with $\alpha = 5$ in the hindrance function. Using $\alpha = 5$, we calculated the RMSE between the predicted and simulated fluxes and stress σ_{22}. The RMSE for the flux prediction is 0.00016 ± 0.00014. Examination of the RMSE for

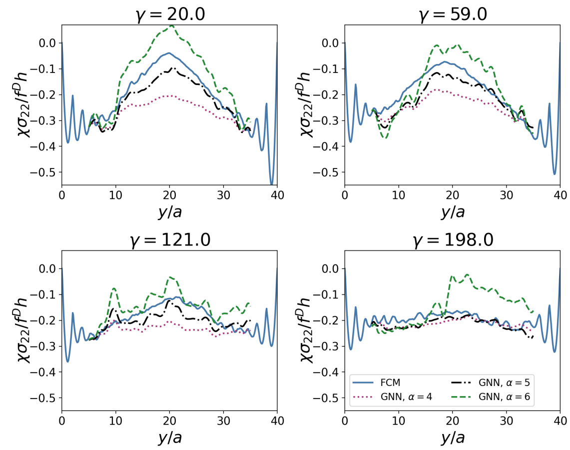

Fig. 17: Stress (σ_{22}) for the monodisperse suspension from FCM and learned stress from the GNN formulation at $\gamma = 20, 59, 121, 198$.

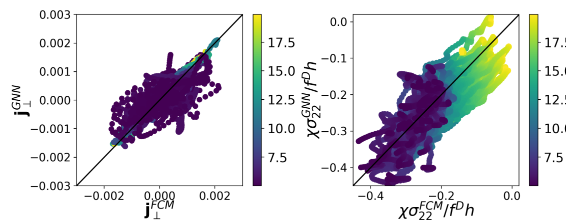

Fig. 18: A comparison of the exact and predicted fluxes (left) and σ_{22}-stress (right) for 62 values of γ evenly distributed in $[20, 198]$ and for $5 \leq y/a \leq 35$.

the flux finds that it is largest for the smallest and largest accumulated strains considered and minimum from $\gamma = 20$ to $\gamma = 150$. Unsurprisingly, the RMSE is smaller than the error found by using the stress data directly in Sec. 5.1, because the GNN methods directly train to match the flux profiles. The RMSE in the stress predictions is 0.0423 ± 0.0185. Plots of a comparison between the predicted and exact fluxes and stresses are given in Fig. 18.

5.3 Learning the stress in bidisperse suspensions

We now consider a bidisperse suspension with particle radii a_S and a_L. We use the bidisperse extension of the monodisperse suspension balance model proposed by Howard et al. (2022). Namely, we consider the system of PDEs:

$$\begin{cases} \frac{2a_L^2}{9\eta_f} f_L(\phi_L, \phi_S) \left(\frac{\partial \sigma_{22,L}}{\partial y}\right) = \mathbf{j}_{\perp,L} & \text{in } \Omega \\ \frac{2a_S^2}{9\eta_f} f_S(\phi_L, \phi_S) \left(\frac{\partial \sigma_{22,S}}{\partial y}\right) = \mathbf{j}_{\perp,S} & \text{in } \Omega \\ \sigma_{22,L}|_{y=y_0} = g_L,\ \sigma_{22,S}|_{y=y_0} = g_S & \text{on } \Gamma, \end{cases} \tag{15}$$

where ϕ_i, $\sigma_{22,i}$, and $\mathbf{j}_{\perp,i}$ are the volume fractions, shear stresses, and fluxes of each phase for $i \in \{L, S\}$. We again assume that particle phase stresses can be approximated by $\sigma_{22,i}$.

The bidisperse suspension balance model from Howard et al. (2022) uses the Shauly et al. (2000) hindrance function f_i due to its simplicity and the possibility of unphysical models with the Davis and Gecol (1994) function. The Shauly et al. (2000) hindrance function is given by

$$f_i(\phi_L, \phi_S) = \frac{1-\phi_i}{\eta_s}, \tag{16}$$

where η_s is the shear viscosity given by

$$\eta_s(\phi) = \left(1 - \frac{\phi}{\phi^c_{\text{bi}}}\right)^{-2} \tag{17}$$

with critical volume fraction ϕ^c_{bi} given by

$$\phi^c_{\text{bi}} = \phi^c_{\text{mono}} \left(1 + c\left|\frac{a_L - a_S}{a_L + a_S}\right|^{3/2} \cdot \left(\frac{\phi_L}{\phi_L + \phi_S}\right)^{3/2} \left(\frac{\phi_S}{\phi_L + \phi_S}\right)\right). \tag{18}$$

The critical volume fraction in the monodisperse case is taken to be $\phi^c_{\text{mono}} = 0.59$ and the parameter $c \approx 1.5$. We note that we also considered the bidisperse hindrance function from Davis and Gecol (1994) for this work, with similar results.

The results from the GNN training are shown in Figs. 19 and 20. We consider only one illustrative example in the interest of space, with $\lambda = 0.6$ and $\beta = 0.75$. In the bidisperse case, the GNN learns the flux accurately. The RMSEs for the learned flux profiles are $8.87 \times 10^{-6} \pm 7.29 \times 10^{-6}$ for large particles and $1.48 \times 10^{-5} \pm 1.01 \times 10^{-5}$. At early times, $\gamma = 20$, the GNN stress agrees well with the simulation data. However, at later times the GNN does not capture the increase in the magnitude of the stress at the channel centerline, particularly for small particles. This is reflected in larger RMSEs, 0.0205 ± 0.0063 for large particles and 0.0519 ± 0.0175 for small particles. Figure 21 shows the large region at the center of the channel, y/a near 20, where the predicted stress, σ_{22}^{GNN}, is smaller than the true stress. This is an example where the physical model available is not able to fully model the physics of the problem. To use physics-informed training, without stress measurements, for the bidisperse case we will need to include extensions of the bidisperse suspension balance model, including, possibly, coupling particle flux and particle stresses between the phases.

While the physics-informed GNN method with the SBM works well in the monodisperse case, it cannot accurately capture the excess stress in the bidisperse case. For this, we turn to an operator learning method.

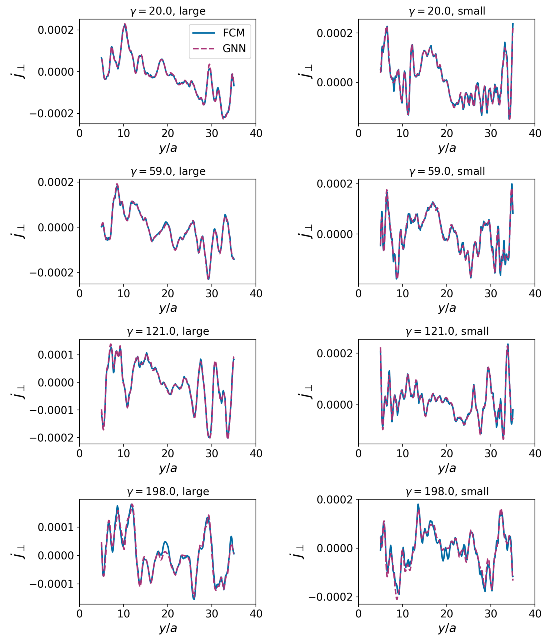

Fig. 19: FCM flux profiles and GNN learned flux profiles at $\gamma = 20, 59, 121$, and 198 calculated with the Shauly et al. (2000) hindrance function for a bidisperse suspension with $\phi_B = 0.4$, $\lambda = 0.6$, and $\beta = 0.75$. Profiles for large particles are in the left column and profiles for small particles are in the right column.

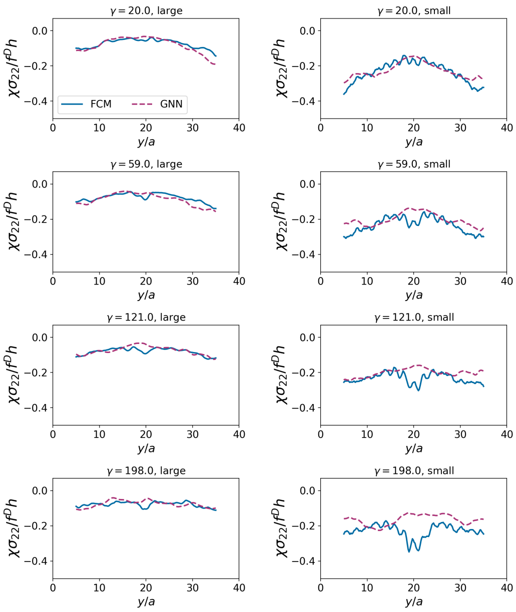

Fig. 20: FCM stress profiles and GNN learned stress profiles at $\gamma = 20, 59, 121, 198$ calculated with the Shauly et al. (2000) hindrance function for a bidisperse suspension with $\phi_B = 0.4$, $\lambda = 0.6$, and $\beta = 0.75$. Profiles for large particles are in the left column and profiles for small particles are in the right column.

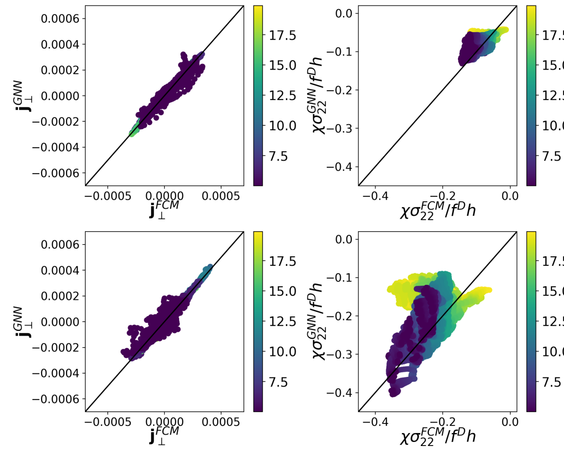

Fig. 21: Comparison between the simulation fluxes (left column) and stresses (right column) and the GNN learned fluxes and stresses for large particles (top row) and small particles (bottom row) for a bidisperse suspension with $\phi_B = 0.4$, $\lambda = 0.6$, and $\beta = 0.75$. The data is plotted for 62 values of γ evenly distributed in $[20, 198]$ and for $5 \leq y/a_L \leq 35$.

6 Data based machine learning for particle stresses

The advantage of the physics-informed training presented in Sec. 5 is that no measurements of the stress profiles are needed. This makes the physics-informed approach uniquely and especially well suited to cases where it is not possible to measure the particle stress, such as in many experimental setups for suspension Poiseuille flows. However, the accuracy of the method depends on the accuracy of the physics-based model being applied, and in cases such as that shown in Sec. 5.3, we cannot learn the stress profiles when the model does not fully capture the physics. Instead, we have to turn to training using data, in the form of stress measurements. In this section, we present an application of operator learning with MOR-physics, which uses measurements of the volume fractions and velocities, along with knowledge of the stress in a training set, to predict the stress for new values of the volume fraction and velocity.

6.1 Learning the stress in suspensions with MOR-Physics

We adopt the following modification to the MOR-Physics operator parameterization to learn σ_{22} from the particle velocities,

$$\mathcal{N}(u_z(t), t) = \mathcal{C}^{-1}(g(\kappa, t;\ \xi_g) \cdot \mathcal{C}h(u_z(t), t;\ \xi_h)) \tag{19}$$

where $\mathcal{C}$ is a discrete cosine transform, $h : \mathbb{R}^n \times \mathbb{R} \to \mathbb{R}^n$ is a deep neural network applied point-wise to the velocity profile, u_z, $g : \mathbb{R} \times \mathbb{R} \to \mathbb{R}$ is a deep neural network applied point-wise to the wavenumber, κ, and ξ_g, ξ_h are the network parameters. $n \in \{1, 2\}$ refers to the number of components of the flow (monodisperse or bidisperse). We obtain a model for the mapping, $(u_z(t), t) \to \sigma_{22}$ by optimizing a least-squares loss,

$$\xi_g, \xi_h = \underset{\hat{\xi}_g, \hat{\xi}_h}{\operatorname{argmin}}\ \|\sigma_{22}(t) - \mathcal{N}(u_z(t), t)\|^2_{\ell^2}. \tag{20}$$

See Appendix A.3 for additional details.

Figures 22 and 23 compare the learned and predicted stresses of the FCM simulations to the MOR-Physics predictions for the $\phi_B = 0.4$ volume fraction monodisperse flow. There is no obvious

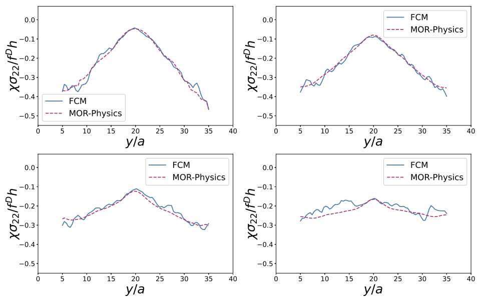

Fig. 22: Monodisperse, $\phi_B = 0.4$, stress profiles from FCM and MOR-Physics learned model for $\gamma = 20, 60, 120, 198$.

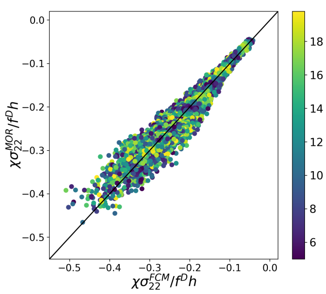

Fig. 23: Comparison between the simulation stresses and the MOR-Physics learned stresses for a monodisperse suspension. The stresses are shown for 90 evenly distributed values of accumulated strain $\gamma \in [20, 200]$ and color-coded according to the position in the channel for $5 \leq y/a \leq 35$.

pattern between the error in the stress prediction and the position in the channel. The RMSE error is 0.0221 ± 0.005.

Figures 24, 25, 26, and 27 compare the stresses from the FCM simulations to the MOR-Physics predictions for the $\phi_B = 0.4$ volume fraction for the three bidisperse flows. For all cases, we can capture the correct time evolution of the stresses with the MOR-Physics models. Importantly, the MOR-Physics model showed the increased stress on the small particles at the channel centerline in the bidisperse suspensions. For the large particle stress predictions, the RMSEs are 0.027 ± 0.005, 0.022 ± 0.004, and 0.015 ± 0.002 for $\beta = 0.25, 0.5,$ and 0.75, respectively. The small particle stress RMSEs are 0.017 ± 0.002, 0.024 ± 0.003, and 0.024 ± 0.003 for $\beta = 0.25, 0.5,$ and 0.75. When

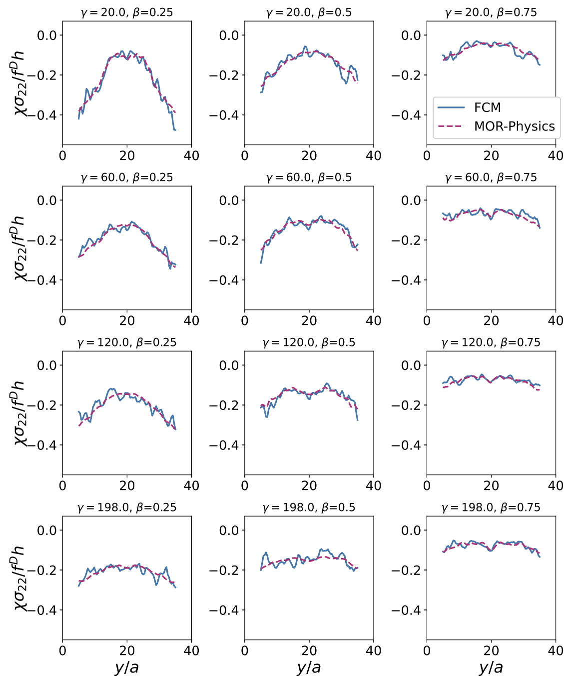

Fig. 24: Bidisperse large particle stress profiles from FCM and MOR-Physics learned model for $\gamma = 20, 60, 120, 198$ and $\beta = 0.25, 0.5, 0.75$. The stresses are shown for 90 evenly distributed values of accumulated strain $\gamma \in [20, 200]$ and color-coded according to the position in the channel for $5 \leq y/a_L \leq 35$.

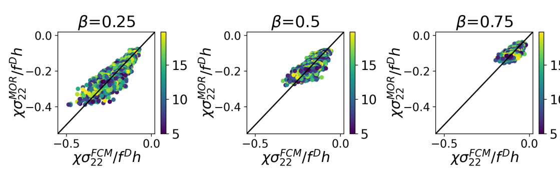

Fig. 25: Comparison between the simulation stresses and the MOR-Physics learned stresses for the large particles in a bidisperse suspension with $\beta = 0.25, 0.5, 0.75$.

we compare with the same case in Sec. 5.3, MOR-Physics learns with a smaller RMSE, particularly for the small particles due to the better agreement at the channel centerline. However, this requires training with stress data, which may be difficult to attain.

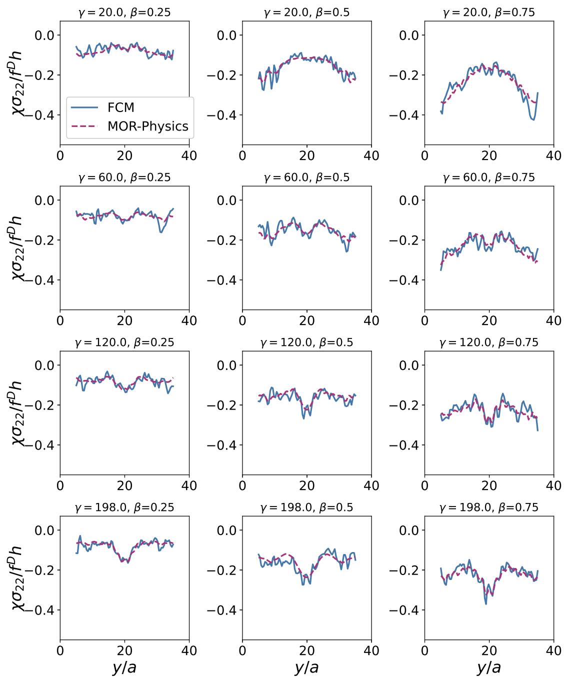

Fig. 26: Bidisperse small particle stress profiles from FCM and MOR-Physics learned model for $\gamma = 20, 60, 120, 198$ and $\beta = 0.25, 0.5, 0.75$.

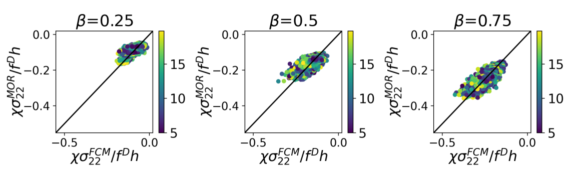

Fig. 27: Comparison between the simulation stresses and the MOR-Physics learned stresses for the small particles in a bidisperse suspension with $\beta = 0.25, 0.5, 0.75$. The stresses are shown for 90 evenly distributed values of accumulated strain $\gamma \in [20, 200]$ and color-coded according to the position in the channel for $5 \leq y/a \leq 35$.

7 Conclusions

In this paper, we have shown that we can learn the complex stress development for monodisperse and bidisperse suspensions through both physics-informed machine learning with the SBM and data-informed operator learning.

One key and exciting prospect for machine learning for rheology is to discover new or higher-order models for fluids. For example, in the bidisperse suspension balance model from Howard et al. (2022), we could consider a coupling term between the two phases in the form of a contribution from the stress of phase b on the flux of phase a by extending Eq. 15 to include a simple coupling between the two fluid phases:

$$\begin{cases} \dfrac{2r_a^2}{9\eta_f} f_a(\phi_a, \phi_b) \left(\dfrac{\partial \sigma_{22,a}}{\partial y} + \varepsilon_{ab} \dfrac{\partial \sigma_{22,b}}{\partial y} \right) = \mathbf{j}_{\perp,a} & \text{in } \Omega \\ \dfrac{2r_b^2}{9\eta_f} f_b(\phi_a, \phi_b) \left(\varepsilon_{ba} \dfrac{\partial \sigma_{22,a}}{\partial y} + \dfrac{\partial \sigma_{22,b}}{\partial y} \right) = \mathbf{j}_{\perp,b} & \text{in } \Omega \\ \sigma_{22,a}|_{y=y_0} = g_a, \ \sigma_{22,b}|_{y=y_0} = g_b & \text{on } \Gamma. \end{cases} \tag{21}$$

The coupling of the phases is controlled by the parameters $0 \leqslant \varepsilon_{ab}, \varepsilon_{ba} \leqslant 1$. When $\varepsilon_{ab} = \varepsilon_{ba} = 0$, Eq. 15 reduces to a decoupled system in which the flux of each particle phase is driven only by the respective particle stresses. While it is not immediately obvious how the phases should be coupled, ε_{ab} and ε_{ba} could be treated like trainable parameters, possibly as a function of the size ratio λ.

Additionally, particles in a suspension form force chains that span significant distances (Gallier et al., 2015) and transmit particle stresses across the channel. In our work, we have seen that in the monodisperse suspension with $\phi_B = 0.4$, approximately half the particles are in contact in one large force chain at later accumulated strains. These force chains lead to long-range coupling of particle movements, where one particle is impacted by not just its nearest neighbors, but other neighbors in the force chain. Due to this long-range nature, suspension rheology may be better modeled by nonlocal counterparts of the traditional local models, which can capture longer-range particle forces naturally (Jin et al., 2014, 2018). Results with a two-phase continuum model to predict the volume fraction evolution have shown that the inclusion of nonlocal stresses leads to better agreement in the core of the channel (Monsorno et al., 2017). Recent work in scientific machine learning for nonlocal equations, such as Barros de Moraes et al. (2023); You et al. (2021, 2020); Pang et al. (2020), has shown that through machine learning algorithms we can discover nonlocal constitutive laws for phenomena that exhibit long-range interactions, including flows.

Additional machine learning will require large, high-quality datasets, ideally publicly available, such as that from (Antolik et al., 2023), and also ideally accompanied by simulations. These datasets are costly to produce. The Johns Hopkins Turbulence Database has enabled the rapid development of data-driven turbulence models (Li et al., 2008; Duraisamy et al., 2019). Large databases for colloidal flows may similarly lead to the discovery of new models. In some cases, training will be improved by multifidelity methods, where lower fidelity data with higher uncertainty is accompanied by a few, high fidelity datasets, and by incorporating physics-informed learning when needed. Physics-informed learning can play a key role because it allows for uncovering quantities that may not be able to be measured. For example, in Sec. 5, we can learn the particle stress from only flux measurements, which are significantly easier to obtain in a laboratory. In a laboratory context, the first step in training would be to recover the flux profile, which could additionally be found from a GNN, using evolving volume fraction data for ϕ. For a unidirectional Poisueille flow, the particle conservation equation gives (Morris and Boulay, 1999)

$$\frac{\partial \phi}{\partial t} + \nabla \cdot \mathbf{j} = 0. \tag{22}$$

Thus, a GNN could be trained using auto-differentiation with Eq. 22 to differentiate in t and integrate in y to find the particle flux profile as a function of streamwise position and time.

In contrast to the physics-informed training, the method in Sec. 6 requires measurements of the particle stress for use in the training set. However, once the model is trained it can be used to obtain the stress of new experiments or simulations, without the need to measure the stress directly. These methods are complementary, and the method chosen should depend on the available data and the fidelity of the accompanying physics-based models. Once obtained, surrogate models may replace expensive high-fidelity simulations or experiments as the inner loop of design optimization or as the low-fidelity estimates in multifidelity uncertainty quantification.

Acknowledgments

The authors thank Dr. Kyongmin Yeo for his contributions to the monodisperse FCM code and helpful discussions.

A.A.H. acknowledges support from the National Science Foundation Graduate Research Fellowship under Grant No. DGE 1058262 and support from the U.S. Department of Energy, Advanced Scientific Computing Research program, under the Scalable, Efficient and Accelerated Causal Reasoning Operators, Graphs and Spikes for Earth and Embedded Systems (SEA-CROGS) project (Project No. 80278), and the Physics-Informed Learning Machines for Multiscale and Multiphysics Problems (PhILMs) project (Project No. 72627). J.D. acknowledges support from the National Science Foundation Mathematical Sciences Graduate Internship Program. The computational work was performed using PNNL Institutional Computing at Pacific Northwest National Laboratory and computational resources and services at the Center for Computation and Visualization, Brown University. R.G.P also acknowledges support from the PhILMs project for this work.

Pacific Northwest National Laboratory (PNNL) is a multi-program national laboratory operated for the U.S. Department of Energy (DOE) by Battelle Memorial Institute under Contract No. DE-AC05-76RL01830.

Sandia National Laboratories is a multimission laboratory managed and operated by National Technology and Engineering Solutions of Sandia, LLC, a wholly owned subsidiary of Honeywell International, Inc., for the U.S. Department of Energy's National Nuclear Security Administration under contract DE-NA0003525. This paper describes objective technical results and analysis. Any subjective views or opinions that might be expressed in the paper do not necessarily represent the views of the U.S. Department of Energy or the United States Government.

Statements and Declarations

The authors declare no competing interests

References

Abbas, M., E. Climent, O. Simonin, and M.R. Maxey. 2006. Dynamics of bidisperse suspensions under Stokes flows: Linear shear flow and sedimentation. *Phys. Fluids* 18: 1–20. https://doi.org/10.1063/1.2396916 .

Adams, R.A. and J.J. Fournier. 2003. *Sobolev spaces*. Elsevier.

Ainsworth, M. and J. Dong. 2021. Galerkin neural networks: A framework for approximating variational equations with error control. *SIAM Journal on Scientific Computing 43*(4): A2474–A2501 .

Antolik, J.T., A. Howard, F. Vereda, N. Ionkin, M. Maxey, and D.M. Harris. 2023. Shear-induced migration of a suspension under quasi-planar confinement. *arXiv preprint arXiv:2302.10380* .

Barros de Moraes, E.A., M. D'Elia, and M. Zayernouri. 2023. Machine learning of nonlocal micro-structural defect evolutions in crystalline materials. *Computer Methods in Applied Mechanics and Engineering* 403: 115743 .

Batchelor, G.K. and J. Van Rensburg. 1986. Structure formation in bidisperse sedimentation. *J. Fluid Mech.* 166: 379–407. https://doi.org/10.1017/S0022112086000204 .

Boodaghidizaji, M., M. Khan, and A.M. Ardekani. 2022. Multi-fidelity modeling to predict the rheological properties of a suspension of fibers using neural networks and gaussian processes. *Phys. Fluids 34*(5): 053101 .

Boyer, F., O. Pouliquen, and É. Guazzelli. 2011. Dense suspensions in rotating-rod flows: normal stresses and particle migration. *J. Fluid Mech.* 686: 5–25. https://doi.org/10.1017/jfm.2011.272 .

Butler, J.E., P.D. Majors, and R.T. Bonnecaze. 1999. Observations of shear-induced particle migration for oscillatory flow of a suspension within a tube. *Phys. Fluids 11*(10): 2865–2877. https://doi.org/10.1063/1.870145 .

Chang, C. 1994. Effect of particle size distributions on the rheology of concentrated bimodal suspensions. *J. Rheol. 38*(1): 85. https://doi.org/10.1122/1.550497 .

Chun, B., I. Kwon, H.W. Jung, and H.C. Hyun. 2017. Lattice Boltzmann simulation of shear-induced particle migration in plane Couette-Poiseuille flow: Local ordering of suspension. *Phys. Fluids 29*(29): 121605–121605. https://doi.org/10.1063/1.4991428 .

Chun, B., J.S. Park, H.W. Jung, and Y.Y. Won. 2019. Shear-induced particle migration and segregation in non-brownian bidisperse suspensions under planar poiseuille flow. *J. Rheol. 63*(3): 437–453 .

Clevert, D.A., T. Unterthiner, and S. Hochreiter. 2015. Fast and accurate deep network learning by exponential linear units (elus). *arXiv preprint arXiv:1511.07289* .

Coussot, P. 1994. Steady, laminar, flow of concentrated mud suspensions in open channel. *Journal of Hydraulic Research 32*(4): 535–559 .

Cui, F.R., A.A. Howard, M.R. Maxey, and A. Tripathi. 2017. Dispersion of a suspension plug in oscillatory pressure-driven flow. *Phys. Rev. Fluids 2*(9): 094303. https://doi.org/10.1103/PhysRevFluids.2.094303 .

Da Cunha, F.R. and E.J. Hinch. 1996. Shear-induced dispersion in a dilute suspension of rough spheres. *J. Fluid Mech.* 309: 211–223 .

Dance, S.L. and M.R. Maxey. 2003. Incorporation of lubrication effects into the force-coupling method for particulate two-phase flow. *J. Comput. Phys.* 189: 212–238. https://doi.org/10.1016/S0021-9991(03)00209-2 .

Davis, P.J. and P. Rabinowitz. 2007. *Methods of numerical integration*. Courier Corporation.

Davis, R.H. and H. Gecol. 1994. Hindered settling function with no empirical parameters for polydisperse suspensions. *AIChE Journal 40*(3): 570–575 .

Dbouk, T., L. Lobry, and E. Lemaire. 2013. Normal stresses in concentrated non-brownian suspensions. *J. Fluid Mech.* 715: 239–272 .

Di Carlo, D. 2009. Inertial microfluidics. *Lab Chip* 9: 3038–3046. https://doi.org/10.1039/b912547g .

Drew, D.A. 1983. Mathematical Modeling of Two-Phase Flow. *Annual Review of Fluid Mechanics* 15: 261–291. https://doi.org/10.1146/annurev.fl.15.010183.001401 .

Drew, D.A. and R.T. Lahey. 1993. Analytical modeling of multiphase flow, In *Particulate Two-Phase Flows*, ed. Roco, M. Butterworth-Heinemann.

Duraisamy, K., G. Iaccarino, and H. Xiao. 2019. Turbulence modeling in the age of data. *Annual Review of Fluid Mechanics 51*(1): 357–377 .

Gadala-Maria, F. and A. Acrivos. 1980. Shear-induced structure in a concentrated suspension of solid spheres. *J. Rheol. 24*(6): 799–814 .

Gallier, S., E. Lemaire, F. Peters, and L. Lobry. 2015. Percolation in suspensions and De Gennes conjectures. *Phys. Rev. E* 92: 020301 .

Gao, C., B. Xu, and J.F. Gilchrist. 2009. Mixing and segregation of microspheres in microchannel flows of mono- and bidispersed suspensions. *Phys. Rev. E 79*(3): 036311. https://doi.org/10.1103/PhysRevE.79.036311 .

Graham, A.L., S.A. Altobelli, E. Fukushima, L.A. Mondy, and T.S. Stephens. 1991. Note: NMR imaging of shear induced diffusion and structure in concentrated suspensions undergoing Couette flow. *J. Rheol. 35*(1): 191–201. https://doi.org/10.1122/1.550227 .

Hampton, R.E., A.A. Mammoli, A.L. Graham, N. Tetlow, and S.A. Altobelli. 1998. Migration of particles undergoing pressure-driven flow in a circular conduit. *J. Rheol. 41*(3): 621. https://doi.org/10.1122/1.550863 .

Harris, C.R., K.J. Millman, S.J. van der Walt, R. Gommers, P. Virtanen, D. Cournapeau, E. Wieser, J. Taylor, S. Berg, N.J. Smith, R. Kern, M. Picus, S. Hoyer, M.H. van Kerkwijk, M. Brett, A. Haldane, J.F. del Río, M. Wiebe, P. Peterson, P. Gérard-Marchant, K. Sheppard, T. Reddy, W. Weckesser, H. Abbasi, C. Gohlke, and T.E. Oliphant. 2020, September. Array programming with NumPy. *Nature 585*(7825): 357–362. https://doi.org/10.1038/s41586-020-2649-2 .

He, L. and D.K. Tafti. 2019. A supervised machine learning approach for predicting variable drag forces on spherical particles in suspension. *Powder technology* 345: 379–389 .

Howard, A., M. Maxey, and K. Yeo. 2018. Settling of heavy particles in concentrated suspensions of neutrally buoyant particles under uniform shear. *Fluid Dyn. Res.* https://doi.org/10.1088/1873-7005/aabfa6 .

Howard, A.A. and M.R. Maxey. 2018. Simulation study of particle clouds in oscillating shear flow. *J. Fluid Mech.* 852: 484–506 .

Howard, A.A., M.R. Maxey, and S. Gallier. 2022. Bidisperse suspension balance model. *Phys. Rev. Fluids 7*(12): 124301 .

Husband, D.M., L.A. Mondy, E. Ganani, and A.L. Graham. 1994. Direct measurements of shear-induced particle migration in suspensions of bimodal spheres. *Rheol. Acta 33*(3): 185–192. https://doi.org/10.1007/BF00437303 .

Jin, H., K. Kang, K. Ahn, W. Briels, and J. Dhont. 2018. Non-local stresses in highly non-uniformly flowing suspensions: The shear-curvature viscosity. *The journal of chemical physics 149*(1): 014903 .

Jin, H., K. Kang, K.H. Ahn, and J.K. Dhont. 2014. Flow instability due to coupling of shear-gradients with concentration: non-uniform flow of (hard-sphere) glasses. *Soft matter 10*(47): 9470–9485 .

Kanehl, P. and H. Stark. 2015. Hydrodynamic segregation in a bidisperse colloidal suspension in microchannel flow: A theoretical study. *J. Chem. Phys. 142*(21): 214901. https://doi.org/10.1063/1.4921800 .

Karniadakis, G.E., I.G. Kevrekidis, L. Lu, P. Perdikaris, S. Wang, and L. Yang. 2021. Physics-informed machine learning. *Nature Reviews Physics 3*(6): 422–440 .

Karnis, A., H. Goldsmith, and S. Mason. 1966. The kinetics of flowing dispersions: I. Concentrated suspensions of rigid particles. *J. Colloid Interface Sci. 22*(6): 531–553. https://doi.org/10.1016/0021-9797(66)90048-8 .

Kingma, D.P. and J. Ba. 2015. Adam: A method for stochastic optimization. *arXiv preprint arXiv:1412.6980* .

Koh, C.J., P. Hookham, and L.G. Leal. 1994. An experimental investigation of concentrated suspension flows in a rectangular channel. *J. Fluid Mech.* 266 .

Leighton, D. and A. Acrivos. 1987. The shear-induced migration of particles in concentrated suspensions. *J. Fluid Mech.* 181: 415–439 .

Lhuillier, D. 2009. Migration of rigid particles in non-Brownian viscous suspensions. *Phys. Fluids 21*(2): 023302. https://doi.org/10.1063/1.3079672 .

Li, Y., E. Perlman, M. Wan, Y. Yang, C. Meneveau, R. Burns, S. Chen, A. Szalay, and G. Eyink. 2008. A public turbulence database cluster and applications to study lagrangian evolution of velocity increments in turbulence. *Journal of Turbulence* 9: N31 .

Li, Z., N.B. Kovachki, K. Azizzadenesheli, B. liu, K. Bhattacharya, A. Stuart, and A. Anandkumar 2021. Fourier neural operator for parametric partial differential equations. In *International Conference on Learning Representations.*

Lomholt, S. and M.R. Maxey. 2003. Force-coupling method for particulate two-phase flow: Stokes flow. *J. Comput. Phys. 184*(2): 381–405. https://doi.org/10.1016/S0021-9991(02)00021-9 .

Lu, L., P. Jin, G. Pang, Z. Zhang, and G.E. Karniadakis. 2021. Learning nonlinear operators via DeepONet based on the universal approximation theorem of operators. *Nature Machine Intelligence 3*(3): 218–229 .

Lyon, M.K. and L.G. Leal. 1998a. An experimental study of the motion of concentrated suspensions in two-dimensional channel flow. Part 1. Monodisperse systems. *J. Fluid Mech.* 363. https://doi.org/10.1017/S0022112098008817 .

Lyon, M.K. and L.G. Leal. 1998b. An experimental study of the motion of concentrated suspensions in two-dimensional channel flow. Part 2. Bidisperse systems. *J. Fluid Mech.* 363. https://doi.org/10.1017/S0022112098008829 .

Maxey, M.R. and B.K. Patel. 2001. Localized force representations for particles sedimenting in Stokes Flow. *Int. J. Muliphase Flow* 27: 1603–1626 .

Metzger, B. and J.E. Butler. 2010. Irreversibility and chaos: Role of long-range hydrodynamic interactions in sheared suspensions. *Phys. Rev. E 82*(5): 51406 .

Metzger, B. and J.E. Butler. 2012. Clouds of particles in a periodic shear flow. *Phys. Fluids 24*(2): 021703. https://doi.org/10.1063/1.3685537 .

Metzger, B., P. Pham, and J.E. Butler. 2013. Irreversibility and chaos: Role of lubrication interactions in sheared suspensions. *Phys. Rev. E 87*(5): 052304. https://doi.org/10.1103/PhysRevE.87.052304 .

Miller, R.M. and J.F. Morris. 2006. Normal stress-driven migration and axial development in pressure-driven flow of concentrated suspensions. *J. Nonnewton. Fluid Mech. 135*(2-3): 149–165. https://doi.org/10.1016/j.jnnfm.2005.11.009 .

Monsorno, D., C. Varsakelis, and M. Papalexandris. 2017. Poiseuille flow of dense non-colloidal suspensions: The role of intergranular and nonlocal stresses in particle migration. *Journal of Non-Newtonian Fluid Mechanics* 247: 229–238 .

Morris, J.F. 2009. A review of microstructure in concentrated suspensions and its implications for rheology and bulk flow. *Rheol. Acta 48*(8): 909–923. https://doi.org/10.1007/s00397-009-0352-1 .

Morris, J.F. and F. Boulay. 1999. Curvilinear flows of noncolloidal suspensions: The role of normal stresses. *J. Rheol.* 43: 1213–1237 .

Nott, P.R. and J.F. Brady. 1994. Pressure-driven flow of suspensions: simulation and theory. *J. Fluid Mech.* 275: 157. https://doi.org/10.1017/S0022112094002326 .

Nott, P.R., É. Guazzelli, and O. Pouliquen. 2011. The suspension balance model revisited. *Phys. Fluids 23*(4): 043304. https://doi.org/10.1063/1.3570921 .

Pang, G., M. D'Elia, M. Parks, and G.E. Karniadakis. 2020. npinns: nonlocal physics-informed neural networks for a parametrized nonlocal universal laplacian operator. algorithms and applications. *Journal of Computational Physics* 422: 109760 .

Patel, R.G. and O. Desjardins. 2018. Nonlinear integro-differential operator regression with neural networks. *arXiv preprint arXiv:1810.08552* .

Patel, R.G., N.A. Trask, M.A. Wood, and E.C. Cyr. 2021. A physics-informed operator regression framework for extracting data-driven continuum models. *Computer Methods in Applied Mechanics and Engineering* 373: 113500 .

Peherstorfer, B. and K. Willcox. 2016. Data-driven operator inference for nonintrusive projection-based model reduction. *Computer Methods in Applied Mechanics and Engineering* 306: 196–215 .

Pesche, R. 1998. *Etude par simulation numerique de la ségrégation de particules dans une suspension bidisperse*. Ph. D. thesis, Université de Nice-Sophia Antipolis, France.

Pesche, R., G. Bossis, and A. Meunier. 1998. Numerical simulation of particle segregation in a bidisperse suspension. *HAL preprint:hal-00694958* .

Pham, P., J.E. Butler, and B. Metzger. 2016. Origin of critical strain amplitude in periodically sheared suspensions. *Phys. Rev. Fluids 1*(2): 022201. https://doi.org/10.1103/PhysRevFluids.1.022201 .

Pham, P., B. Metzger, and J.E. Butler. 2015. Particle dispersion in sheared suspensions: Crucial role of solid-solid contacts. *Phys. Fluids 27*(5): 051701. https://doi.org/10.1063/1.4919728 .

Phillips, R.J., R.C. Armstrong, R.A. Brown, A.L. Graham, and J.R. Abbott. 1992. A constitutive equation for concentrated suspensions that accounts for shear-induced particle migration. *Phys. Fluids 4*(1): 30–40. https://doi.org/10.1063/1.858498 .

Pivkin, I.V., P.D. Richardson, and G. Karniadakis. 2006. Blood flow velocity effects and role of activation delay time on growth and form of platelet thrombi. *Proc. Natl. Acad. Sci. U. S. A. 103*(46): 17164–9. https://doi.org/10.1073/pnas.0608546103 .

Raissi, M., P. Perdikaris, and G.E. Karniadakis. 2019. Physics-informed neural networks: A deep learning framework for solving forward and inverse problems involving nonlinear partial differential equations. *J. Comp. Phys.* 378: 686–707 .

Reyes, B., A.A. Howard, P. Perdikaris, and A.M. Tartakovsky. 2021. Learning unknown physics of non-newtonian fluids. *Phys. Rev. Fluids 6*(7): 073301 .

Richardson, J.F. and W.N. Zaki. 1954. The sedimentation of a suspension of uniform spheres under conditions of viscous flow. *Chem. Eng. Sci. 3*(2): 65–73. https://doi.org/10.1016/0009-2509(54)85015-9 .

Sarabian, M., M. Firouznia, B. Metzger, and S. Hormozi. 2019. Fully developed and transient concentration profiles of particulate suspensions sheared in a cylindrical couette cell. *J. Fluid Mech.* 862: 659–671 .

Schroen, K., A. van Dinther, and R. Stockmann. 2017. Particle migration in laminar shear fields: A new basis for large scale separation technology? *Separation and Purification Technology* 174: 372–388 .

Semwogerere, D., J.F. Morris, and E.R. Weeks. 2007. Development of particle migration in pressure-driven flow of a Brownian suspension. *J. Fluid Mech.* 581: 437. https://doi.org/10.1017/S0022112007006088 .

Semwogerere, D. and E.R. Weeks. 2008. Shear-induced particle migration in binary colloidal suspensions. *Phys. Fluids 20*(4): 043306. https://doi.org/10.1063/1.2907378 .

Servais, C., R. Jones, and I. Roberts. 2002. The influence of particle size distribution on the processing of food. *J. of Food Engineering 51*(3): 201–208 .

Shauly, A., A. Wachs, and A. Nir. 2000. Shear-induced particle resuspension in settling polydisperse concentrated suspension. *Int. J. Multiphase Flow 26*(1): 1–15 .

Sirignano, J. and K. Spiliopoulos. 2018. Dgm: A deep learning algorithm for solving partial differential equations. *J. Comp. Phys.* 375: 1339–1364 .

Snook, B., J.E. Butler, and É. Guazzelli. 2016. Dynamics of shear-induced migration of spherical particles in oscillatory pipe flow. *J. Fluid Mech 786*(5): 128–153. https://doi.org/10.1017/jfm.2015.645 .

Wang, Y., J. Ouyang, and X. Wang. 2021. Machine learning of lubrication correction based on gpr for the coupled dpd–dem simulation of colloidal suspensions. *Soft Matter 17*(23): 5682–5699 .

Yeo, K. 2011. *Some aspects of suspension flows: Stokes to turbulent flows.* Ph. D. thesis, Brown University.

Yeo, K. and M.R. Maxey. 2010a. Dynamics of concentrated suspensions of non-colloidal particles in Couette flow. *J. Fluid Mech.* 649: 205. https://doi.org/10.1017/S0022112009993454 .

Yeo, K. and M.R. Maxey. 2010b. Simulation of concentrated suspensions using the force-coupling method. *J. Comput. Phys. 229*(6): 2401–2421. https://doi.org/10.1016/j.jcp.2009.11.041 .

Yeo, K. and M.R. Maxey. 2011. Numerical simulations of concentrated suspensions of monodisperse particles in a Poiseuille flow. *J. Fluid Mech.* 682: 491–518 .

You, H., Y. Yu, S. Silling, and M. D'Elia. 2020. Data-driven learning of nonlocal models: from high-fidelity simulations to constitutive laws. *arXiv preprint arXiv:2012.04157* .

You, H., Y. Yu, N. Trask, M. Gulian, and M. D'Elia. 2021. Data-driven learning of nonlocal physics from high-fidelity synthetic data. *Computer Methods in Applied Mechanics and Engineering* 374: 113553 .

Yu, B. et al. 2018. The deep ritz method: a deep learning-based numerical algorithm for solving variational problems. *Communications in Mathematics and Statistics 6*(1): 1–12 .

Zarraga, I.E. and D.T. Leighton. 2002. Measurement of an unexpectedly large shear-induced self-diffusivity in a dilute suspension of spheres. *Phys. Fluids 14*(7): 2194. https://doi.org/10.1063/1.1483304 .

A Appendix

A.1 Additional bidisperse suspension plots

In this section, we provide figures analogous to Figs. 7–11 for bidisperse suspensions with $\phi_B = 0.4$, $\lambda = 0.6$, and $\beta = 0.5$ (Figs. 28–30) and $\beta = 0.25$ (Figs. 33–35).

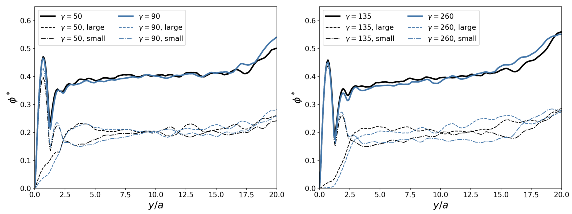

Fig. 28: Volume fraction profiles at accumulated strain $\gamma = 0 - 260$ for $\phi_B = 0.4$, $\lambda = 0.6$, and $\beta = 0.5$. The volume fraction is averaged of the channel center line at $y/a = 20.0$. The $(\cdot)^*$ notation denotes the profile is averaged over four reseeded simulations, as discussed in Sec. 2.1.

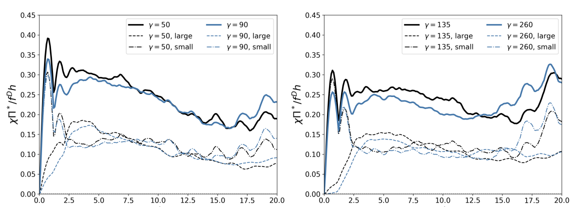

Fig. 29: Particle contact pressure profiles as defined by Eq. 4 at accumulated strain $\gamma = 0-260$ for $\phi_B = 0.4$, $\lambda = 0.6$, and $\beta = 0.5$.

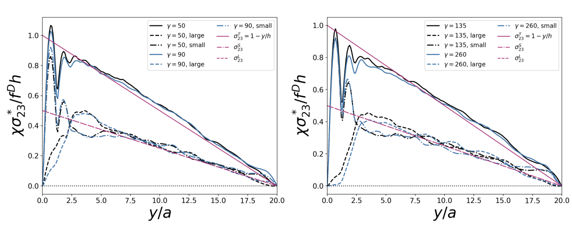

Fig. 30: Shear stress profiles for $\phi_B = 0.4$, $\lambda = 0.6$, and $\beta = 0.5$.

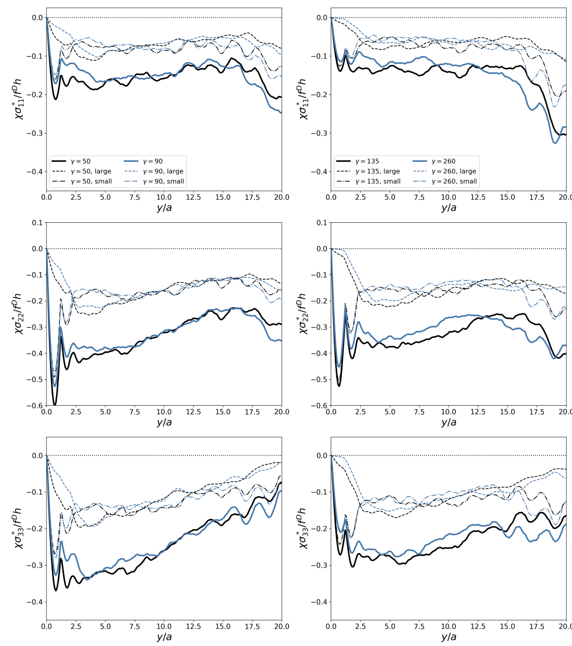

Fig. 31: Stress profiles σ_{11} (top), σ_{22} (middle), and σ_{33} (bottom) for bidisperse steady flows of particles for $\phi_B = 0.4$, $\lambda = 0.6$, and $\beta = 0.5$, and for $\gamma = 0 - 260$.

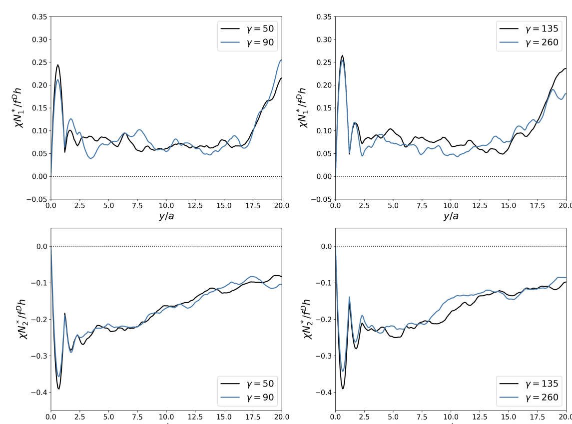

Fig. 32: Normal stress difference profiles for monodisperse steady flows of particles for $\phi_B = 0.4$, $\lambda = 0.6$, and $\beta = 0.5$.

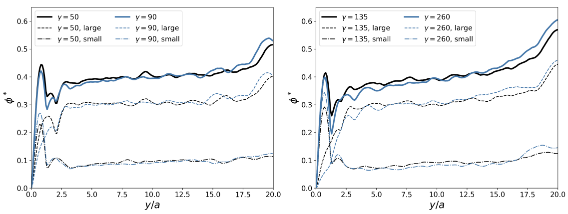

Fig. 33: Volume fraction profiles at accumulated strain $\gamma = 0 - 260$ for $\phi_B = 0.4$, $\lambda = 0.6$, and $\beta = 0.25$. The volume fraction is averaged of the channel center line at $y/a = 20.0$. The $(\cdot)^*$ notation denotes the profile is averaged over four reseeded simulations, as discussed in Sec. 2.1.

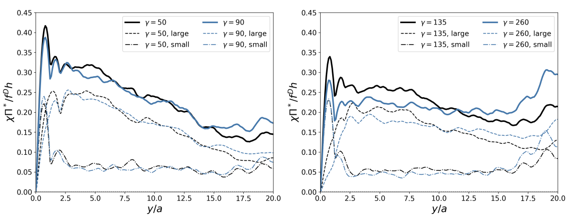

Fig. 34: Particle contact pressure profiles as defined by Eq. 4 at accumulated strain $\gamma = 0-260$ for $\phi_B = 0.4$, $\lambda = 0.6$, and $\beta = 0.25$.

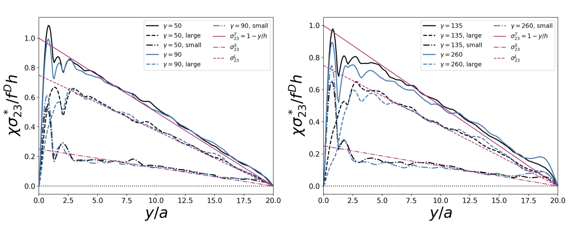

Fig. 35: Shear stress profiles for $\phi_B = 0.4$, $\lambda = 0.6$, and $\beta = 0.25$.

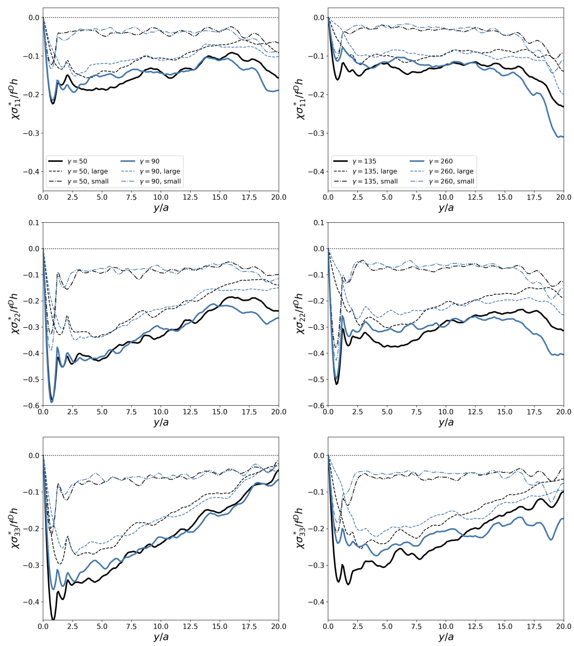

Fig. 36: Stress profiles σ_{11} (top), σ_{22} (middle), and σ_{33} (bottom) for bidisperse steady flows of particles for $\phi_B = 0.4$, $\lambda = 0.6$, and $\beta = 0.25$, and for $\gamma = 0 - 260$.

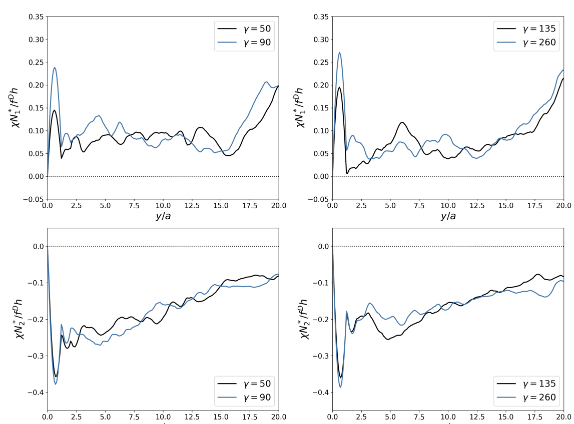

Fig. 37: Normal stress difference profiles for monodisperse steady flows of particles for $\phi_B = 0.4$, $\lambda = 0.6$, and $\beta = 0.25$.

A.2 Galerkin Neural Network Implementation

In order to apply Galerkin Neural Networks to the SBM formulation in Sec. 5.2, we must first formulate it as a variational problem whose operator is symmetric and positive-definite. To accomplish this, we use a simple least squares variational approach:

$$\begin{aligned}
&\sigma_{22} \in L^2(\Omega_\gamma;\ H^1(\Omega_y))\ : \\
&\int_\Omega \frac{2a^2}{9\eta_f} f(\phi)\frac{\partial \sigma_{22}}{\partial y} \cdot \frac{2a^2}{9\eta_f} f(\phi)\frac{\partial \tau}{\partial y}\ d\Omega \\
&\quad + C\int_{\Omega_\gamma} \sigma_{22}\cdot\tau\ d\Omega_\gamma \\
&\quad = \int_\Omega \mathbf{j}_\perp \cdot \frac{2a^2}{9\eta_f} f(\phi)\frac{\partial \tau}{\partial y}\ d\Omega \qquad \forall \tau \in L^2(\Omega_\gamma;\ H^1(\Omega_y)).
\end{aligned}$$

The space $L^2(\Omega_\gamma;\ H^1(\Omega_y))$ is the Sobolev space (Adams and Fournier, 2003) of all functions u such that

$$||u||_{L^2(\Omega_\gamma;\ H^1(\Omega_y))} := \left(\int_{\Omega_\gamma} ||u(\gamma,\cdot)||^2_{H^1(\Omega_y)}\ d\Omega_\gamma\right)^{1/2}$$

is finite, where

$$||v||_{H^1(\Omega_y)} := (||v||^2_{L^2(\Omega_y)} + ||\nabla_y v||^2_{L^2(\Omega_y)})^{1/2}.$$

For ease of notation, we define

$$\begin{aligned}
a(\sigma,\tau) &:= \int_\Omega \frac{2a^2}{9\eta_f} f(\phi)\frac{\partial \sigma_{22}}{\partial y} \cdot \frac{2a^2}{9\eta_f} f(\phi)\frac{\partial \tau}{\partial y}\ d\Omega \\
&\qquad + C\int_{\Omega_\gamma} \sigma_{22}\cdot\tau\ d\Omega_\gamma \\
L(\tau) &:= \int_\Omega \mathbf{j}_\perp \cdot \frac{2a^2}{9\eta_f} f(\phi)\frac{\partial \tau}{\partial y}\ d\Omega.
\end{aligned}$$

Here, $C > 0$ is a constant that determines how strongly the boundary condition is enforced. We take $C = 0.1$ in all examples.

The basis function Σ_i^{NN} is obtained by solving the following optimization problem:

$$\Sigma_i^{NN} = \underset{\tau\in\mathcal{NN}}{\arg\max}\ \frac{L(\tau) - a(\sigma_{22,i-1},\tau)}{a(\tau,\tau)^{1/2}}, \tag{23}$$

where $\mathcal{NN}$ denotes the set of all realizations of a feedforward neural network of fixed width and depth. We denote by $\sigma_{22,i}$ the ith approximation to σ_{22} using the first i basis functions $\{\Sigma_j^{NN}\}_{j=1}^i$; $\sigma_{22,i}$ is obtained by solving the discrete variational problem

$$\sigma_{22,i} \in S_i\ :\quad a(\sigma_{22,i},\tau) = L(\tau)\quad \forall\tau\in S_i,$$

where $S_i = \text{span}\{\Sigma_0^{NN}, ..., \Sigma_i^{NN}\}$. We take $\sigma_{22,0}$ to be the initial approximation to the PDE and set $\Sigma_0^{NN} := \sigma_{22,0}$. For all of the simulations in Section 5, we take $\sigma_{22,0} = 0$. This choice of initial approximation means that we do not assume any prior knowledge of the solution. One can of course use a more informed initial approximation if it exists, e.g. coarse result from another numerical method.

To evaluate the loss functional in Eq. 23, we approximate the integrals using high-order Gaussian quadrature rules such as the ones described in Davis and Rabinowitz (2007). In particular, for a given function $g : \Omega \to \mathbb{R}$, we use the quadrature rule given by the weights $\{w_i\}_{i=1}^m$ and nodes $\{(y_i,\gamma_i)\}_{i=1}^m$ as follows:

$$\int_\Omega g(y,\gamma)\ d\Omega \approx \sum_{i=1}^m w_i g(y_i,\gamma_i). \tag{24}$$

The key idea behind Galerkin Neural Networks is the approximation $\Sigma_i^{NN} \approx \sigma_{22} - \sigma_{22,i-1}$ – that is, the ith basis function is an estimate of the error in the approximate solution $\sigma_{22,i-1}$. As the error $\sigma_{22} - \sigma_{22,i-1}$ decreases, its structure grows increasingly complex and contains high frequency modes. Thus, the first basis functions may be viewed as approximating low frequency error components while later basis functions approximate high frequency error components. A discussion and demonstration of the hierarchical nature of Galerkin Neural Networks alongside theoretical properties may be found in Ainsworth and Dong (2021).

A.3 MOR-Physics parameters

In this section, we provide additional details for the MOR-Physics operator parameterization used in Section 6. To perform training, we first partition the FCM simulations into 60% training data, 20% validation data, and 20% test data. Over the course of training, we track the validation loss and select the operator with the lowest validation loss as our learned operator. Below we list the hyperparameters we used in the studies,

Hyperparameter	Value
DNN width	64
DNN depth	32
DNN activation function	ELU (Clevert et al., 2015)
optimizer	Adam (Kingma and Ba, 2015)
learning rate	10^{-3}
training steps	10000